

An Analysis of Cloud Cover and Water Vapor for the ALMA Project:

**A Comparison Between Chajnantor (Chile), Chalviri
(Bolivia) and Five Sites in Argentina
using Satellite Data and a Verification of Satellite
PWV measurements**

A Report
to
European Southern Observatories

by

D. André Erasmus, Ph.D.
(Certified Consulting Meteorologist)

Final Report
31 December, 2002

Purchase Order
66814/ODG/02/6419/GWI/LET

1. Introduction

This report presents the results of a study for the Atacama Large Millimeter Array (ALMA) Project. In the first part of the study a 5-year satellite data set was used to analyze and compare cloud cover and water vapor at Chajnantor (Chile), Chiviriviri (Bolivia) and four sites in Argentina. Since time was of the essence in completing this part of the study, it was proposed that the site comparison be undertaken using the methodology employed in an earlier study by Erasmus and van Staden (2001). This action implied that a verification (validation) of the satellite-derived precipitable water vapor (PWV) measurement using independent ground-based observations at Chajnantor could not be completed before the site comparison. The results of the site comparison were presented in a meeting at European Southern Observatory (ESO) headquarters in Garching on 15 July, 2002. At this meeting a request was made by ESO representatives (Drs Massimo Tarenghi and Marc Sarazin) for additional work. This included adding a fifth site in Argentina and a variation in the computation of the site quality indicators.

Subsequently a verification of the satellite PWV measurement has been undertaken using rawinsonde data and 183GHz radiometer data from Chajnantor. This verification is important for two reasons. Firstly, it validates the results of the site comparison and secondly, it is an essential precursor to the implementation of the operational cloud cover and PWV forecast service for ALMA at Chajnantor in 2003. In the process of doing the verification study, discrepancies were detected in the radiometer data record. Following an investigation and communication with ESO representatives (Marc Sarazin, Roberto Rivera) a cleaned radiometer data set was obtained. The verification was then completed. The results indicate that the satellite PWV computed using the methodology of Erasmus and van Staden (2001) is in good agreement with contemporaneous rawinsonde and radiometer observations. Thus the results of the site comparison have been validated. When only the satellite and radiometer data were compared (a larger data set) greater disagreement between the observations was found. The nature of the disagreement suggests that the cleaned radiometer data set still contains questionable observations.

This report is structured in logical rather than chronological order. Section 2 outlines the methodology used to derive cloud cover and water vapor parameters from the satellite data. Section 3 presents the results of the comparison between satellite, rawinsonde and radiometer PWV measurements at Chajnantor. The site comparison (with additions and revisions to the 15 July, 2002 interim report) can be found in section 4.

2. Methodology

In this study, measurements of water vapor and cloud were derived from meteorological satellite observations made by passive remote sensing at different wavelengths (Figure 1). At infra-red (IR) wavelengths, the satellite measures the monochromatic emittance of the earth and atmosphere at 10.7 μ m (IR window) and at 6.7 μ m, a water vapor absorption band. Depending on the wavelength of the emissions being measured by the satellite, different quantities can be derived. Figure 2 shows the weighting functions for different IR channels.

In the IR window channel, emissions reach the satellite largely unattenuated by the atmosphere so that radiance values measured are due to emission from the surface.

However, clouds absorb and emit essentially as blackbodies at infra-red wavelengths. The result is that, when clouds are present in the atmosphere, these behave as an elevated emitting “surface” so that radiation reaching the satellite is from the cloud top.

Water vapor in the atmosphere is absorbent at most infra-red wavelengths. The absorptivity for a given wavelength determines the layer in the atmosphere in which out-going terrestrial radiation will be absorbed and re-emitted by resident water vapor. Figure 2 indicates that observations at $6.7\mu\text{m}$ are sensitive to water vapor emissions from the layer between 600mb and 300mb. (There are only small amounts of water vapor above 300mb. See Figure 3) Emission from this layer depends on the amount of water vapor in the layer and temperature and is typically calibrated in terms of the relative humidity. An independent upper-air temperature measurement is needed to derive an absolute humidity from the relative humidity. This is accomplished using observed temperature versus height data from rawinsondes or numerical models.

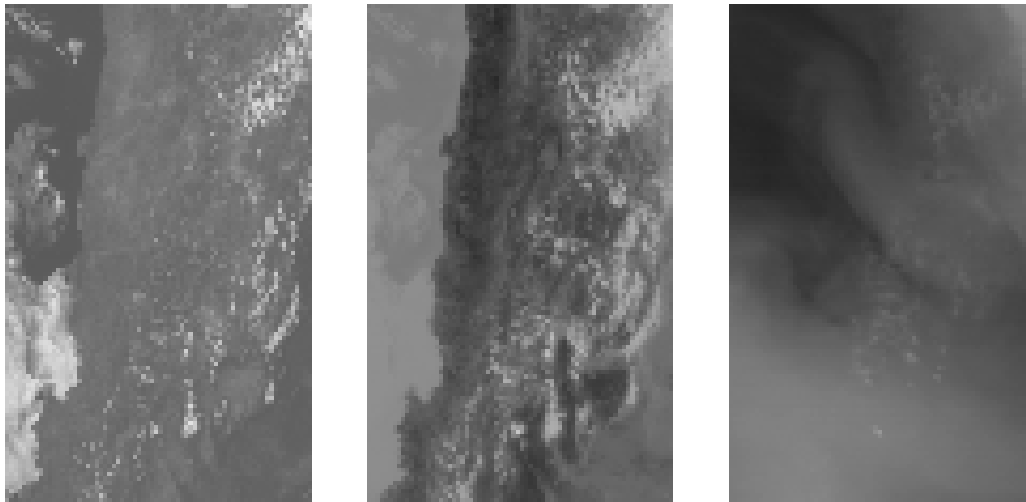


Figure 1. Sample ISCCP satellite images sectors of the area ($20.5^{\circ}\text{S} - 30.5^{\circ}\text{S}$ and $66^{\circ}\text{W} - 72^{\circ}\text{W}$) on January 28, 1996 at 15:11UT. From left to right: Visible channel ($0.55\mu\text{m}$), Infra-red window channel ($10.7\mu\text{m}$) and Water vapor channel ($6.7\mu\text{m}$).

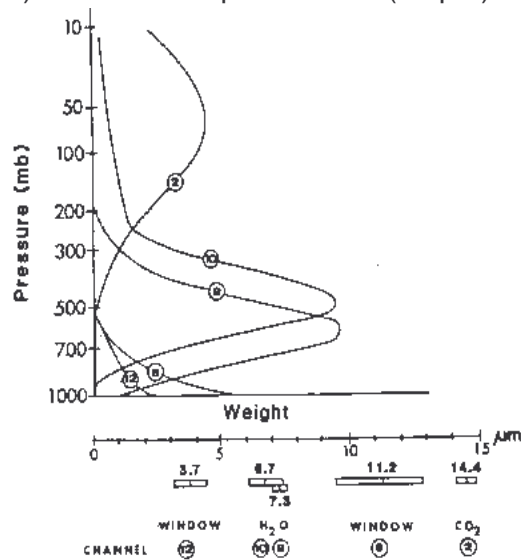


Figure 2. Weighting functions for IR observing channels (from Rao *et al.*, 1990)

2.1 Conversion of radiance to brightness temperature

In the real-time (raw) data stream for the GOES-8 satellite, radiance counts are 10-bits in length for the imager channels. In order to maintain compatibility with older data sets such as GOES-7 and Meteosat-3, these have been scaled into 8-bit counts by ISCCP. The infra-red channel calibration consists of a bias scaling factor and a first order gain scaling factor. True radiance values are obtained using the equation:

$$R = (X - b)/m, \quad (1)$$

where R is radiance ($\text{mW}/[\text{m}^2 \cdot \text{sr} \cdot \text{cm}^{-1}]$) and X is the count value. The coefficients b and m are the scaling bias and the scaling gain, respectively. For the IR window channel, in order to get an accurate temperature of the emitting surface, R must be adjusted to account for absorption by water vapor between the surface and the satellite. In dry areas, particularly for high altitude locations, this correction is negligible. R^* , the adjusted radiance, depends on the precipitable water vapor (PWV) and is given by $R^* = R/\vartheta$ where:

$$\vartheta = -0.0163(\text{PWV}) + 1.0119 \quad (2).$$

The brightness (or effective) temperature is then obtained by inverting the Planck function as follows:

$$T_{\text{eff}} = (c_2 \cdot \nu) / \ln(1 + [c_1 \cdot \nu^3] / R^*) \quad (3)$$

where T_{eff} is effective temperature (K), "ln" stands for natural logarithm and ν (cm^{-1}) is the central wave number of the channel. The coefficients c_1 and c_2 are the two radiation constants and have values of $c_1 = 1.191066 \times 10^{-5}$ ($\text{mW} \cdot \text{m}^{-2} \cdot \text{sr}^{-1} \cdot \text{cm}^4$) and $c_2 = 1.438833$ (cm.K). To convert effective temperature to actual temperature T(K), the following formula is used:

$$T = b \cdot T_{\text{eff}} + a \quad (4)$$

The constants a (K) and b depend on the observation channel. These are bias and gain adjustments that account for variations in the inverse Planck function across the spectral passband of the channel. The differences between the values of T and T_{eff} increase with decreasing temperature. They are usually of the order of 0.1 K and hence negligible for most calculations.

2.2 Conversion of 6.7 μm brightness temperature to UTH

The Upper Tropospheric Humidity (UTH) is a measure of the relative humidity of a layer extending from 600mb (~ 4400m) to 300mb (~ 9000m). For GOES data, Soden and Bretherton (1993, 1996) have derived a semi-empirical relationship between UTH and 6.7 μm channel brightness temperature in clear areas. It is important to note, therefore, that water vapor parameters derived from satellite observations are valid under clear conditions.

The basic form of the relationship is:

$$\text{UTH} = [\exp(a + b \cdot T) \cdot \text{Cos } \theta] / p_0 \quad (5),$$

where θ is the satellite viewing zenith angle, a and b are the least squares fit slope and intercept of the regression line as defined by the empirical relationship and p_0 is a normalized pressure variable.

$$p_0 = p(T=240K) / 300, \tag{6}$$

where p (in mb) is the pressure level where the temperature (T) is 240K. The values for a and b are seasonally dependent and are obtained from a table listing their values for each month of the year. For the ISCCP data from Meteosat-3 the UTH calibration done by Erasmus and van Staden (2001) was applied.

2.3 Computation of precipitable water vapor

The precipitable water vapor (PWV) is a quantity indicating the absolute humidity in the atmosphere above some predetermined altitude such as the surface or a constant pressure level. PWV is derived from the satellite-based UTH measurement. Since the UTH is a measure of the relative humidity in the layer between 300mb and 600mb, for pressure levels between 300mb and 600mb the relative humidity is set equal to the UTH. Then the corresponding mixing ratio (x), the mass of water vapor per mass of air (Kg/Kg), at each level (10mb increments were used) can be computed as follows:

$$x = \text{UTH} \cdot x_s \tag{7}$$

x_s , the saturation mixing ratio, is the maximum water vapor capacity of the air at a given temperature and pressure. Mean monthly rawinsonde data for Antofagasta are used to compute x_s . These are 10-year averages based on daily soundings at 00UT and 12UT from 1977 to 1986. For the verification presented in section 3, since the surface pressure at Chajnantor is lower than 600mb, no assumptions need to be made about the mixing ratio profile at higher pressure levels (lower altitudes). Thus good agreement between the satellite and ground-based measurements of PWV may be expected. Also, since all the sites being compared (Section 4) have a surface altitude greater than 4400m the same would hold true for these sites.

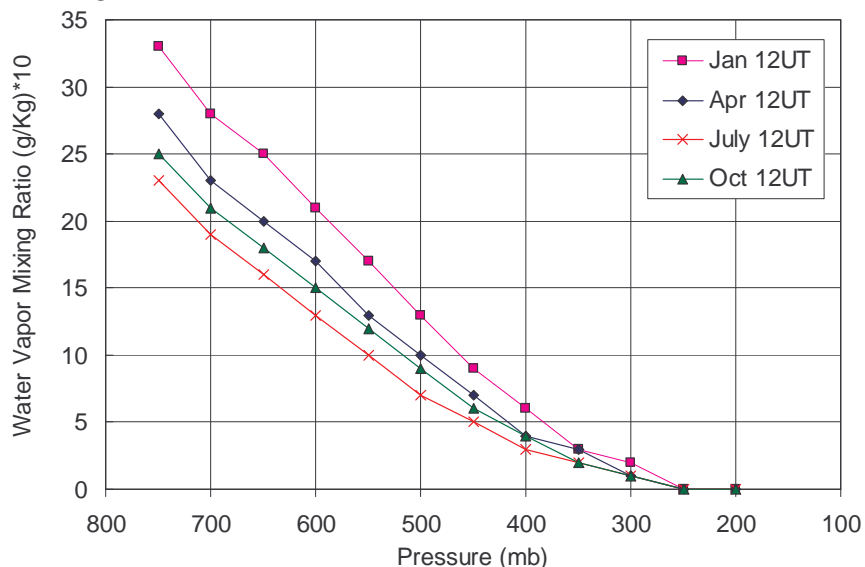


Figure 3. Mean monthly water vapor mixing ratio versus pressure (height) profiles as determined from the Antofagasta rawinsonde for the 10 year period 1977-1986.

To determine the mixing ratio at pressure levels below 300mb the 300mb value is scaled to lower pressure levels using the mean monthly mixing ratio profiles from the Antofagasta rawinsonde. Figure 3 shows the average mixing ratio profiles for four months in the year as derived from the Antofagasta rawinsonde. The profiles exhibit good linearity with pressure (height). It is also clear that the contribution to total PWV from levels above 300mb is very small. Once the mixing ratio profile is obtained, then,

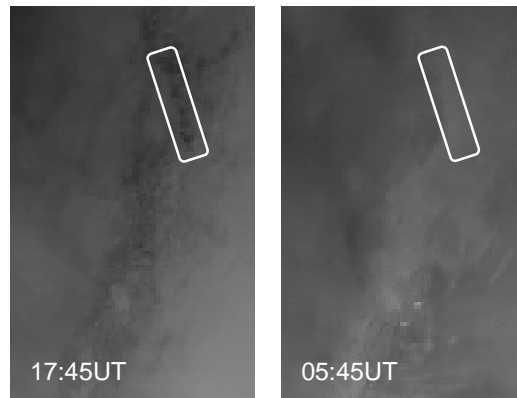
$$PWV = (1/g) \int_0^p x.dp \quad (8)$$

where dp is the incremental pressure change with height in Pascals and g is the gravity acceleration constant. The units for PWV are then kg.m⁻² or mm of water.

Cold surfaces at high altitude have an impact on the computation of PWV. The effect occurs at sites above the 600mb (~4400m) pressure level under very dry conditions at night. At 6.7µm, the satellite senses emissions from the layer between 600mb and 300mb. Therefore, if the surface extends above the 600mb level, emission from the surface may be measured if the air above the surface is extremely dry. An example is shown in Figure 4.

In general, for 6.7µm measurements, a very dry 600mb - 300mb layer will result in a high brightness temperature being measured by the satellite since emissions reaching the satellite would be from the atmosphere below 600mb where temperatures are warm. The low-end detection threshold for UTH therefore corresponds to a warm brightness temperature. For this reason, the presence of a warm elevated surface (daytime conditions) does not pose a problem in the computation of PWV.

Figure 4. Water vapor channel images for June 3-4, 1998 showing the effect of cold surfaces at high altitude under very dry conditions. Note how the high altitude areas west of the Salar de Atacama that are dark (dry) in the daytime image appear light (relatively moist) in the nighttime image.



However, if the ground is cold, emissions from such a cold surface reaching the satellite will produce a relatively low brightness temperature which will be interpreted as a relatively high humidity. Erasmus and van Staden (2001) found that in the analysis of the 6.7µm data, this effect causes PWV values below 1mm to be overestimated at night for high altitude sites. PWV statistics for Chajnantor were determined using 5 years of satellite data (images every three hours) and are shown in Table 1 for four periods defined by dividing, respectively, the day-time and nighttime hours in half. The significantly larger nighttime PWV values for dry conditions (10th percentile and 1st quartile) are caused by the effect described above.

Table 1. Primary statistics of satellite-derived PWV (mm) for Chajnantor for different periods of the day and night.

Period	10 th Percentile	1 st Quartile	Median	3 rd Quartile
Day 1	0.385	0.588	0.860	1.265
Day 2	0.395	0.578	0.871	1.251
Night 1	0.625	0.795	1.084	1.415
Night 2	0.701	0.881	1.155	1.501

In order to assess the magnitude of actual differences (if any) between day and night PWV values, satellite PWV was analyzed at Paranal (a low altitude site which is unaffected by the problem mentioned above) and a location at the latitude of Chajnantor (-23.0°) at the Chilean coast (-71.0°). The primary PWV statistics for these two locations are presented in Tables 2 and 3.

Table 2. Primary statistics of satellite-derived PWV (mm) for Paranal showing day and night differences at a low altitude site with no ground effects. PWV values are for the layer of the atmosphere above the site.

Period	10 th Percentile	1 st Quartile	Median	3 rd Quartile
Day	1.833	2.670	4.090	6.005
Night	1.972	2.862	4.309	6.196

Table 3. Primary statistics of satellite-derived PWV (mm) for a coastal location west of Chajnantor (-23.0°, -71.0°) showing day and night differences in the absence of any ground effects. PWV values are for the layer of the atmosphere above 5000m.

Period	10 th Percentile	1 st Quartile	Median	3 rd Quartile
Day	0.403	0.666	1.088	1.658
Night	0.463	0.751	1.166	1.785

The statistics for PWV show differences between day and night of about 10%. This difference is not real, however, since it may be attributed to the timing of the rawinsonde soundings used in the PWV computation. These soundings are made at 00:00UT (19:00LST) and 12:00UT (07:00LST) daily. The 00UT sounding is used for the second half of the day and first half of the night and the 12UT sounding for the second half of the night and first half of the day. It is apparent that, on average, the actual temperatures in the day will be warmer than the sounding temperatures and *vice versa* at night. In computing x_s (equation 7) and hence PWV, values will be underestimated in the day and overestimated at night. In the free atmosphere day-night air temperatures typically fluctuate 1°C at 500mb. Such a variation in temperature would produce a 9% change in the value of x_s and hence PWV. This effect explains basically all of the day-night difference in PWV values. It is therefore concluded that day-night variations in PWV are negligible. This observation is consistent with the fact that water vapor in the free atmosphere varies on large time and space scales since it is controlled by the movement of large-scale circulations.

In view of the above, in the PWV analysis to be carried out for the site comparisons, daytime PWV values will be used. These measurements are free of the ground effects that may occur at high altitude sites at night and may be considered a representative measure of atmospheric water vapor that can be compared at the selected sites. It should be kept in mind that daytime satellite PWV values are slightly underestimated (~ 5%) due to the timing of the rawinsonde soundings.

Further validation of the satellite PWV measurements may be found in section 3 of this report where the results of a comparison between satellite, rawinsonde and radiometer measurements of PWV at Chajnantor is presented.

2.4 Cloud detection and classification

The presence of cirrus (high altitude) clouds and their thickness is inferred from the 6.7 μ m imagery. Since these clouds are found at an altitude (9-12km) higher than the water vapor emission layer, IR radiation from water vapor below the 300mb level is absorbed and re-emitted at colder temperatures by the cloud particles. According to Wallace and Hobbs (1977), the median heterogeneous freezing temperatures for cloud droplets 0.1mm and 1mm in diameter are, respectively, about -32°C and -25°C. Antofagasta rawinsonde data indicates that typical air temperatures at the 300mb pressure level range from -32°C in summer to -39°C in winter. Therefore clouds identified in the 6.7 μ m imagery, especially thin cirrus, would most likely be ice clouds.

The relationship between UTH and water vapor brightness temperature defined in section 2.2 is valid under clear conditions. When UTH values rise to around 50%, cirrus cloud particles start forming (the cloud particles may not be visible at this stage). UTH measurements continue to be valid in the presence of these microscopic particles. As UTH values rise further, the cloud particles grow in size and number and transparent cirrus cloud becomes visible. For UTH values above 50%, therefore, the UTH is an indicator of cirrus cloud thickness. The transition from transparent to opaque cirrus occurs when the UTH reaches 100% (Erasmus and Sarazin 2000, 2002). For the purposes of cirrus cloud identification and classification the UTH threshold values are as follows:

Clear: $UTH \leq 50\%$
Opaque: $UTH \geq 100\%$
Transparent: $50\% < UTH < 100\%$

Once the opaque cirrus cloud threshold is reached, it is not possible to distinguish any other cloud at lower levels. At 400mb, the Antofagasta rawinsonde temperatures vary from about -17°C in summer to -23°C in winter. This shows that a thick layer of cirrus cloud extending from the 300mb level down to the 400mb level is likely to contain super-cooled water droplets. Therefore, a reasonable and conservative assumption is that liquid water is present in opaque cirrus clouds.

The 10.7 μ m channel data are used to detect cloud at lower levels in the troposphere. Based on the discussion above these clouds would contain liquid water droplets. Pixel temperatures (T_{ir}) computed from the 10.7 μ m satellite data are compared to an estimated surface temperature (T_s). Using the rawinsonde data (geopotential heights of pressure surfaces) and the terrain height the surface pressure (P_s) is estimated by

interpolation. In turn, T_s is estimated. If T_{ir} is colder than T_s , the presence of cloud is indicated. However, T_s is, in effect, the free air temperature at the altitude of the site. The actual surface temperature may be warmer or colder than T_s since the ground undergoes additional cooling (night) or warming (day). If the estimated surface temperature is cooler than the actual surface temperature (day-time) cloud detection is not compromised. However, if the actual temperature is colder than the estimated surface temperature (T_s) and $T_{ir} < T_r = T_s$, then two conditions are possible - cloud may be present or the ground is cold and is incorrectly being interpreted as cloud. In order to avoid this problem a T_r must be used that is lower than T_s when the actual surface temperature is colder than T_s . At the same time the difference between T_r and T_s must be minimized so that cloud, if it is near the ground, does not go undetected.

Erasmus and van Staden (2002), have devised a method which optimizes the value of T_r under the conditions described above. The pressure level (altitude) on which T_r is based is determined by applying a pressure level compensation to P_s that is modeled in terms of the night length. A solar time clock was used to compute the local apparent time of the satellite image (t_{si}), sunrise (t_{sr}), and sunset (t_{ss}). From this information the length of the night (t_{nl}), was computed. A reference time of one hour after sunrise ($t_{sr} + 1$) was determined to be the time when ground detection problems are no longer evident from the night before. The number of hours between the reference time and the satellite image time ($t_{sr} + 1 - t_{si}$) was computed and a pressure level compensation is derived that must be subtracted from P_s to find the pressure level on which T_r is based. This approach is effective in avoiding the mistaken identification of cold ground as cloud while at the same time minimizing the thickness of the layer near the ground in which cloud can not be detected.

Satellite observations of cloud cover using the methodology described above have been compared with independent ground-based observations at Paranal and San Pedro Martir observatories over extended periods (9-12 months) (Erasmus and van Staden, 2001, 2002). At each site the clear fractions determined using the two methods were found to be in good agreement, differing by about 2% (Table 4).

Table 4. Clear fractions for San Pedro Martir Observatory (June 1997 to May 1998) and Paranal Observatory (January - August, 1998) as determined by satellite and ground-based observations.

Clear fraction	SPM (%)	Paranal (%)
Satellite	69.8	82.9
Ground	67.5	80.9

The sky cover classifications described in the previous paragraphs (clear, transparent, opaque) are applied to individual pixels. A more realistic depiction of the astronomical “sky” is obtained by using a cluster of pixels to represent the site. As shown schematically in Figure 5, a 9-pixel area may be used. At the level of the Tropopause (about 12km), for an observer on the ground at 4km altitude viewing the sky, this 9-pixel area would correspond to the sky within approximately 60° of zenith.

For ALMA it is important to know not just if clouds are present, but also if these clouds consist of ice or water particles. For other applications additional distinctions

may be valuable. For these reasons, in this study, three primary sky cover categories were defined with two of these categories having further subcategories as follows:

Clear: All 9 pixels are clear (no ice or water cloud)

Transparent Ice Cloud

I1: 1-3 pixels have transparent ice cloud

I2: 4-6 pixels have transparent ice cloud

I3: 7-9 pixels have transparent ice cloud

Opaque Water Cloud

W1: 1-3 pixels have opaque water cloud

W2: 4-6 pixels have opaque water cloud

W3: 7-9 pixels have opaque water cloud

The procedure for classification is that the opaque pixel count is checked first and if one or more opaque pixels were detected then the sky cover is classified W1, W2 or W3. If no opaque pixels were present, the number of transparent pixels was counted and the sky cover classified as either I1, I2 or I3. Finally, if all the pixels were clear then the sky cover was classified Clear.

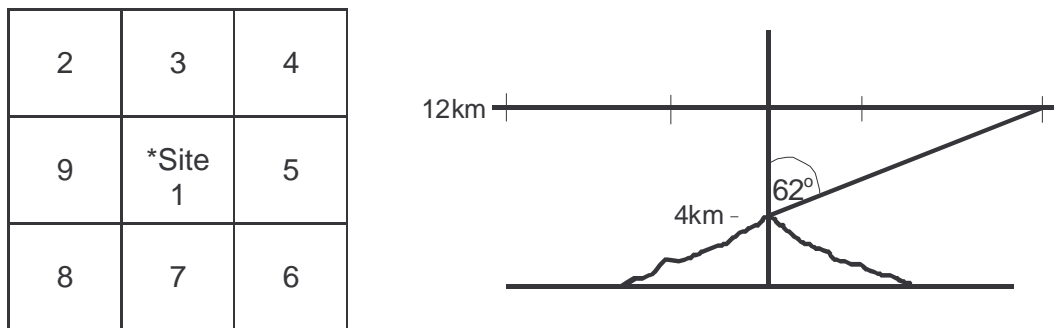


Figure 5. Schematic showing the 9-pixel site area in plan view (left) and cross-section (right). At left, each square represents a 10km x 10km pixel in the satellite image (North is towards the top of the page). The numbers shown in the figure are used to reference the pixel locations. At right, assuming a site altitude of 4km, at Tropopause level (approximately 12km), the “sky” encompassed by the 9-pixels corresponds approximately to an area of observation within 62° of zenith.

3. Verification of satellite PWV measurements

The verification of satellite PWV measurements was based on data collected in the period October 1998 – December 1999. During this period coincident ground-based observations of PWV are available for Chajnantor. The satellite PWV computation was based on full-resolution GOES-8 data and upper-air meteorological data from the European Center for Medium-range Weather Forecasting (ECMWF). These data were those used in producing the cloud cover and water vapor forecasts for Paranal and La Silla and then archived. The methodology described in section 2.3 was applied. For the satellite PWV the pixel (8 km x 8 km) located closest to Chajnantor is used. The satellite image time stamp corresponds to the starting time of the full earth disk scan made by the satellite which is done in a line-by-line mode from north

to south. In synchronizing the satellite observations with ground-based measurements allowance is made for the fact that the satellite takes 26 minutes to complete the scan so that Chajnantor is being observed by the satellite 18.1 minutes after the satellite image time.

Atmospheric opacity measurements have been made at Chajnantor using ground-based radiometers operated by National Radio Astronomy Observatory (NRAO) (225 GHz tipping radiometer) and ESO (183 GHz radiometer). The NRAO radiometer data consists of a direct opacity measurement and no conversion to PWV has been made using an atmospheric model and meteorological data. Delgado *et al.* (1999) have converted the 183 GHz radiometer measurement to PWV using a simple atmospheric model and surface meteorological data for the period October 1998 – December 1999. These data were obtained and compared with the satellite PWV measurements made over the same period. Following an initial comparison (visual inspection of time series plots), inconsistencies and discrepancies were observed between the two data sets. For selected periods the satellite and radiometer data tracked very well. These were interspersed with periods where the radiometer PWV values were persistently near zero or exhibited magnitudes and fluctuations that did not match the satellite data. This matter was referred to ESO (Marc Sarazin and Roberto Rivera) and subsequently a cleaned radiometer data set was obtained. The results of the comparison between the satellite and radiometer PWV values using the cleaned radiometer data set are presented in section 3.2

Starting in October 1998, a series of rawinsonde campaigns were conducted through collaborative efforts at Chajnantor. Rawinsondes launched at or near the site provide measurements of temperature and humidity above the surface from which the PWV can be computed. The campaigns that overlapped with the period of the satellite and processed radiometer data were conducted in October-December 1998, March 1999 and November 1999. About 110 launches were made in this period but not all have valid data from the surface to 9000m (the typical limit for integration in the computation of PWV). Additionally, for the purposes of comparison, observation times were required to be within one hour of each other. Consequently, for the satellite-rawinsonde comparison, 52 pairs of observations were obtained and for the radiometer-rawinsonde comparison, 31 pairs of observations. The comparison of the three different measurement methods based on these contemporaneous data is presented in the next section.

3.1 Comparison of satellite, rawinsonde and radiometer PWV

The 183 GHz radiometer at Chajnantor is located on the plateau area at an altitude of 5050m. This is also the approximate altitude at which ALMA would be built at the site. Accordingly, the satellite and rawinsonde PWV were computed for the atmosphere above 5050m. As noted above, synchronization requires that observations are within one hour of each other. For the radiometer PWV a 60 minute average (10 minute observations) centered on the synchronization time is used in the analysis presented below. Use of a 20 minute average or the nearest value yielded the same results.

Figure 6 shows that the three methods of measurement are highly correlated. For all three combinations of measurement method, the Pearson correlation coefficients (r) are greater than 0.9. Statistical tests (z and t) show that r values this large are significant at the 1% level (less than a 1% probability the correlation is due to a

chance deviation in the sample). In terms of the zero point, best agreement is observed between the satellite and rawinsonde. For the other combinations, those involving the radiometer data, an offset of about 0.3 mm is observed. In both cases the radiometer shows a positive offset.

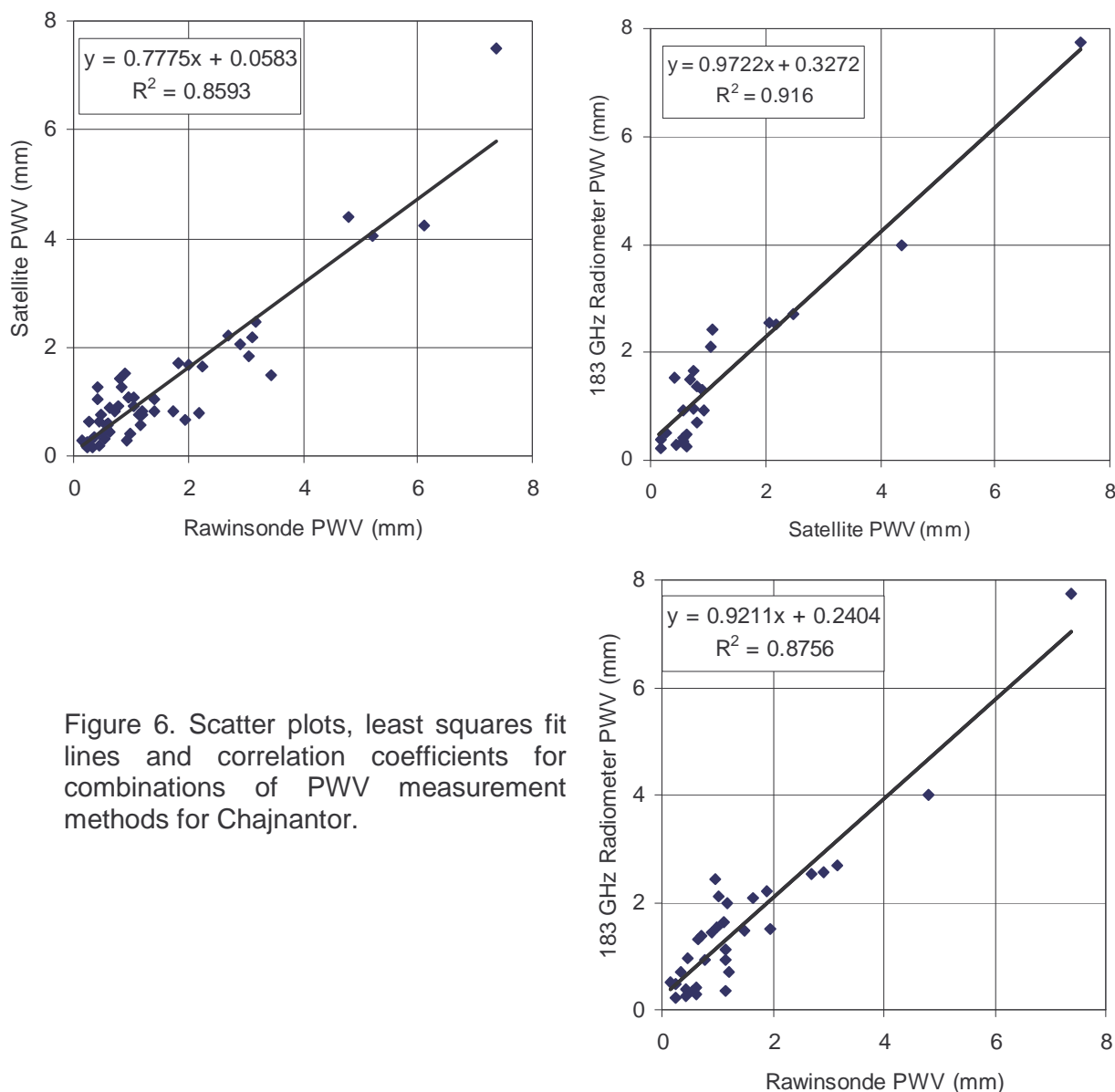


Figure 6. Scatter plots, least squares fit lines and correlation coefficients for combinations of PWV measurement methods for Chajnantor.

3.2 Comparison of satellite and radiometer PWV (expanded data set)

As noted above, PWV measurements derived from the 183 GHz radiometer data are for the period October 1998 – December 1999 (457 days). However the record is not continuous, with radiometer observations available for all or part of only 317 days during this period. Satellite observations are scheduled every three hours but, on an intermittent basis, one or more of the image scans may be cancelled per day for satellite housekeeping procedures. Of 3656 possible scan times, data are available for 2904. Of these, cloud was present on 492 occasions. In order to eliminate the possibility of cold ground effects contaminating the satellite observations (see section 2.3), the scan times 05:45UT, 08:45UT and 11:45UT were excluded from the comparison, leaving 1499 useable satellite PWV observations.

For the comparison of the satellite and radiometer PWV observations there were 979 pairs of synchronous data points. A scatter diagram of these points, the least squares fit regression line and the correlation coefficient are shown in Figure 7. The agreement between the two measurement methods is poorer for the expanded data set but the Pearson correlation coefficient (r) value of 0.6 is still significant at the 1% level.

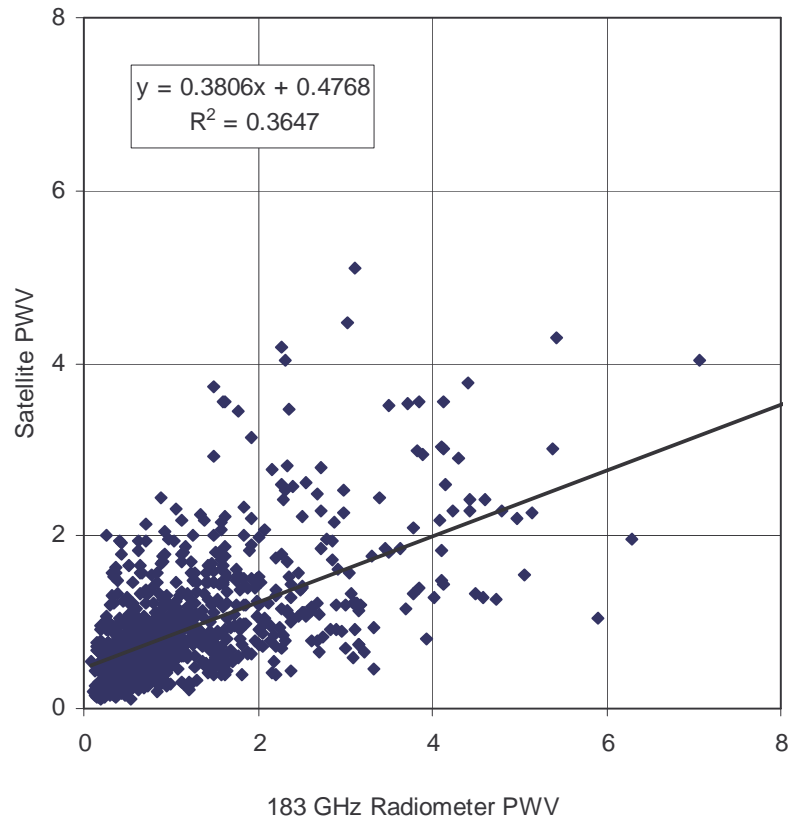


Figure 7. Scatter plot, least squares fit regression line and correlation coefficient for satellite and radiometer measurement of PWV (mm) at Chajnantor using an expanded data set.

The noticeably poorer agreement for the expanded data set was examined further. One unusual feature in the scatter plot is the large number of near zero radiometer PWV values that correspond to satellite PWV measurements ranging from zero to 2mm. This feature in the data creates a large offset of about 0.5mm and no doubt also affects the correlation.

A time series plot of the data was constructed and is presented in the Appendix with each graph showing approximately 45 days. Examination of these graphs reveals that there are periods of very good agreement between the satellite and radiometer but that large differences are sometimes observed. In the period October – December 1998 agreement is generally good. Differences are greater when the PWV is high. It is likely that the atmospheric model used to compute PWV from the raw radiometer data performs poorly under these conditions since a simplified profile of moisture above the surface was assumed and only surface observations were used.

Similar behavior is observed early in 1999 but there appears to be an additional anomalous diurnal oscillation in the radiometer data between days 1 and 24. In 1999 from day 121 onwards there are intermittent periods where the radiometer PWV is near zero while the satellite PWV varies significantly (eg. Days 123-134). Towards the end of 1999 (days 288-355) good agreement is again observed. In this report it would be inappropriate to speculate about the causes for these inconsistencies. However, their existence should be noted since a possible implication is that the radiometer data and/or the method of conversion from opacity to PWV may not be reliable.

4. Site Comparison

4.1 Background

A survey of cloud cover and water vapor over Northern Chile using five years of satellite data was recently completed for Cerro-Tololo Inter-American Observatory (CTIO) and University of Tokyo (UT) (Erasmus and van Staden, 2001). This study mapped the aerial distribution of cloud and PWV over the study area (20.5°S to 30.5°S and 66.0°W to 72.0°W) and quantitatively compared conditions at 14 sites (including Chajnantor) in Northern Chile. While no sites in Bolivia and Argentina were considered in the above mentioned study, the satellite image sectors corresponding to the study area cover the high altitude areas in Bolivia and Argentina near their borders with Chile. Sites in Argentina were selected on the basis of ALMA construction requirements and the aerial distribution of cloud cover and water vapor over the study area as determined by Erasmus and van Staden (2001). ALMA construction requires a flat area $1\text{km} \times 1\text{km}$ without obstacles for the compact array and an area $10\text{km} \times 10\text{km}$ with 50% at a slope less than 5% and 100% with a slope less than 10%. A digital elevation model was used to identify flat areas that match these criteria as closely as possible.

PWV and cloud cover distribution maps for the area are shown in Figures 8 and 9 respectively.

Figure 8. Percentage frequency of occurrence of PWV values below 0.5 mm (left) and below 1.0 mm (right) under clear conditions.

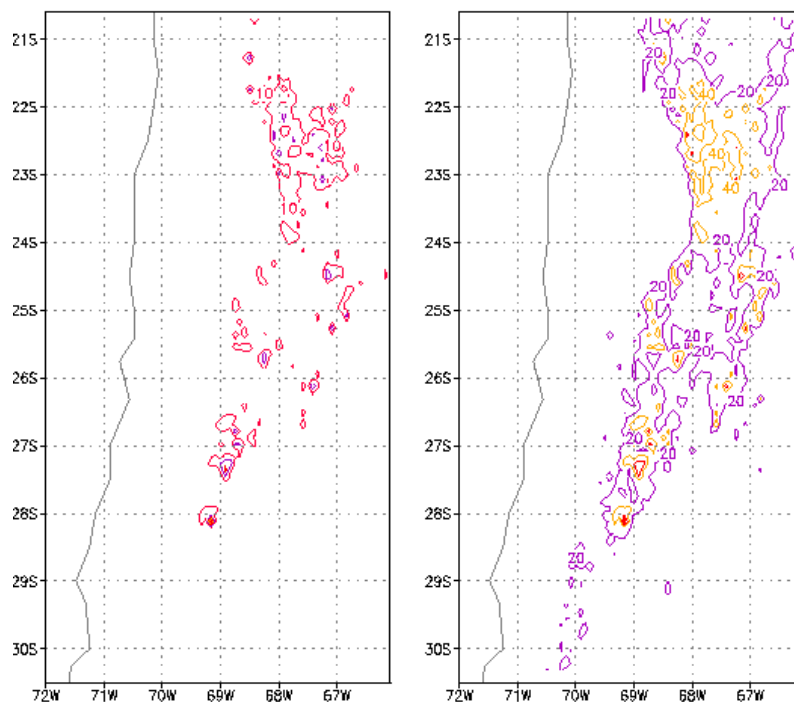


Figure 8 shows that PWV above a given location is controlled to a very large degree by altitude. Higher sites are dryer because the scale height for water vapor in the atmosphere is small. Additionally, higher sites are colder and in cold air the equilibrium water vapor pressure occurs at lower absolute humidities. Accordingly, the driest sites (highest frequency of low PWV values) are located on the Andean Altiplano. It should be noted that PWV values shown in Figure 8 are valid under clear conditions. The maps of PWV should, therefore, be evaluated in the light of the cloud cover distributions shown in Figure 9. Also of significance in interpreting Figure 8 is the fact that digital terrain heights were used in computing PWV for mapping purposes. Since the actual terrain altitude at a particular site may be different and since PWV depends strongly on site altitude the maps shown in Figure 8 were only used for general aerial assessment. In the analysis and comparison of specific sites the actual terrain heights were used.

The cloud cover distribution maps (Figure 9) show that the general pattern of cloud cover is for cloudiness to increase towards the east and south. The latitudinal minimum is between 21.5°S and 24.5°S. The north-south extent of the clearest zone decreases towards the east. At 69°W the minimum is at 23°S. Between 22°S and 24°S the largest west-east gradient in cloud cover occurs between 68°W and 69°W. Morning hours are clearest. Dramatic increases in cloud cover are observed in the afternoon east of the Andes in association with the development of convective storms in this area. The impact of increased afternoon cloudiness extends west of the Cordillera due to local convection and the movement of cloud from the east under certain meteorological conditions. After sunset, clearing is observed east of the Andes as the convection subsides. However, west of about 68°W clearing during the night is gradual and slight. This suggests that the diurnal cycle of cloud cover in this area is controlled mostly by the movement of cloud produced to the east of the Andes into the region rather than by local convection.

Consideration of the PWV and cloud cover maps leads to the conclusion that the clearest and driest sites in Argentina will be as high and as far west as possible. Unfortunately, sites that are sufficiently high and large tend to be located east of 68°W. In terms of cloud cover and water vapor this is not optimal since the steepest gradient of cloud cover is found west of 68°W. Given the information and considerations mentioned above, four sites were initially selected (Arg High, Arg Mid, Arg South and Arg Low). Following preliminary analysis the site Arg West was added. Arg West appears to have the best possible location in Argentina in terms of cloud cover and PWV but it does not fully meet the ALMA site requirements for construction. Table 5 presents the site locations and information. Figure 10 shows the positions of the sites on a topography map.

Table 5. Site locations and information

No	Site	Latitude	Longitude	Size (kmxkm)	Altitude (m)	Max altitude
1	Chajnantor	-22.983	-67.629	10 x 10	5000	5639
2	Chalviri	-22.508	-67.716	10 x 7	5200	5780
3	Arg High	-25.065	-66.945	4 x 3	5100	5355
4	Arg Mid	-25.385	-66.746	8 x 5	4900	5163
5	Arg South	-26.540	-67.887	10 x 6	4900	5308
6	Arg Low	-24.073	-67.434	> 10 x 10	4400	5665
7	Arg West	-25.171	-68.313	4 x 4	5200	5400

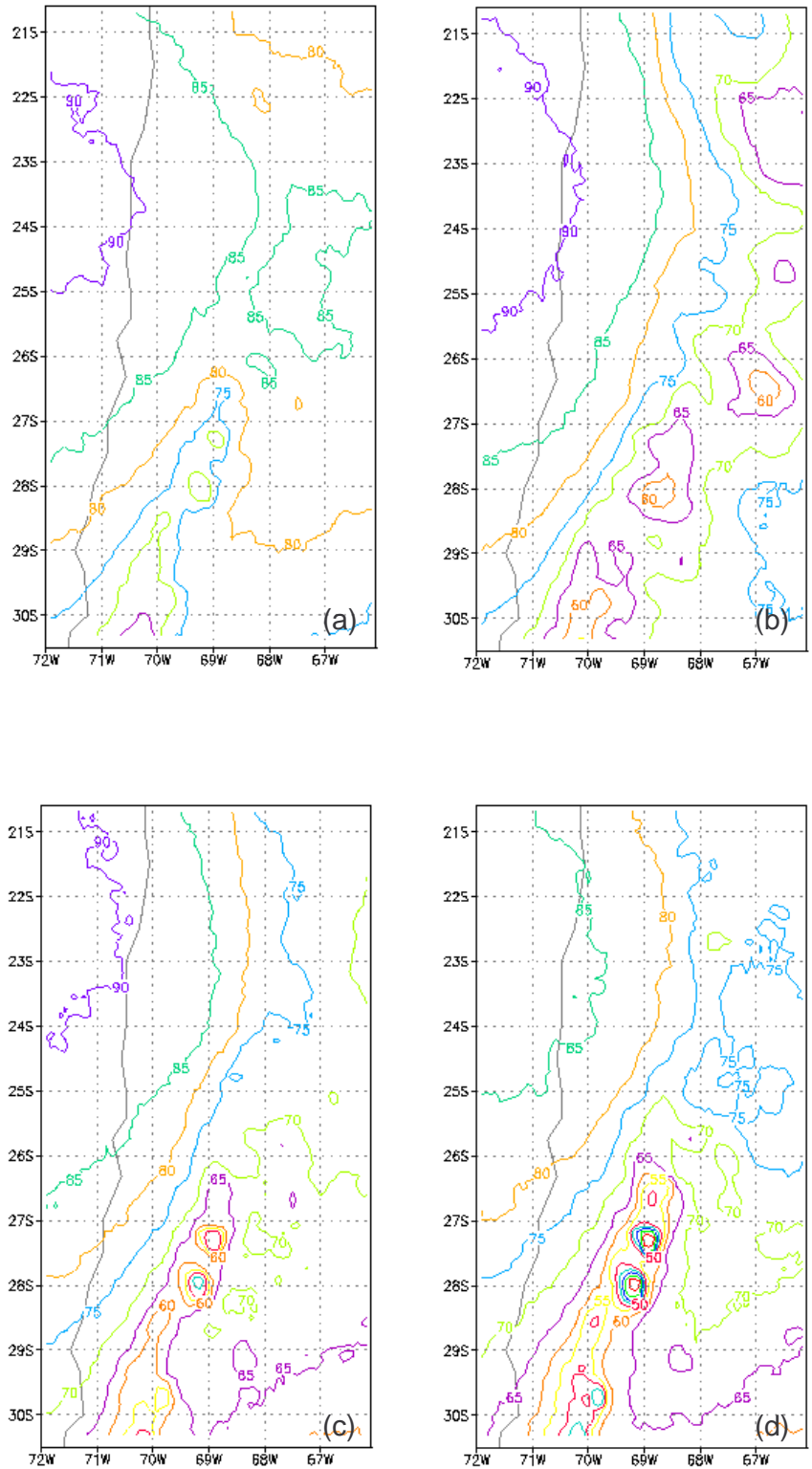


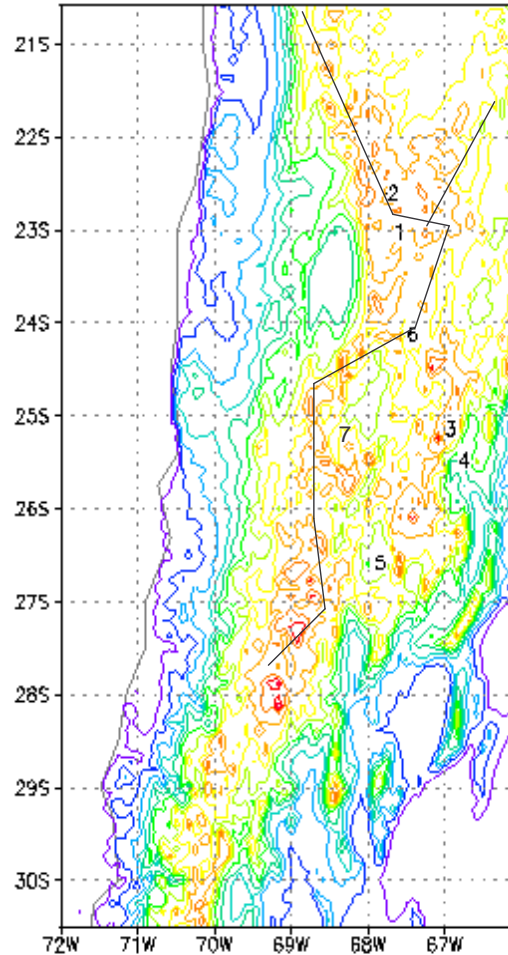
Figure 9. Maps showing the fraction (%) of time that skies are clear for different periods of the day. (a) First half of the day, (b) Second half of the day, (c) First half of the night and (d) second half of the night.

Figure 10. Locations of the sites in Chile, Bolivia and Argentina that were compared using satellite data. Contours show the topography at 500m intervals (see Table 5).

4.2 The Data

The 6.7 μm (water vapor) and 10.7 μm (IR window) satellite imagery used in this study are from the International Satellite Cloud Climatology Project (ISCCP) data set. Five years of satellite data covering the period July 1, 1993 to February 28, 1996 and June 1, 1997 to August 31, 1999 were purchased from the U.S. National Climatic Data Center (NCDC) by Cerro-Tololo Inter-American Observatory (CTIO) and University of Tokyo (UT). A data use agreement between these parties and ESO facilitates the use of these data for this study.

Full earth satellite scans are scheduled every three hours. However, cancellation of one or more images per day occurs periodically due to satellite housekeeping procedures, satellite maneuvers, eclipse events and switches to rapid scan mode during the Northern Hemisphere summer. The data for the study area were extracted from the full earth scans and compiled in a separate database.



The format of the ISCCP data (Campbell, *et. al*, 1997) is a mixture of McIDAS (www.ssec.wisc.edu/software/mcidas.html) format and documentation data transmitted directly from the satellite. The basic structure of the data set is a header containing sector specifications, navigation constants and calibration coefficients. This is followed by scan lines of data from the multi-spectral imager interlaced by pixel. Each scan line is preceded by an 80 byte header which includes the time of the scan.

The first part of the header provides information on the image sector data to follow such as the limits of the scan area, time of scan, channels included, spatial resolution and byte positions for the start of each data section. The next section of the header contains the parameters required for input to the software used to navigate the image areas. A program which converts pixel location to latitude-longitude position with an accuracy of 4km was provided by the National Environmental Satellite Data Information Service (NESDIS). The calibration section of the header provides the data needed to convert the radiance counts to true radiances. Meteosat and GOES perform real-time calibrations of infra-red detectors on-board the satellite using sensor readings from dark space and reference blackbodies. Calibration coefficients thus derived are used to compute radiance values from the raw counts. Further information on the computation of radiance values and derived parameters is given in section 2.3.

In order to determine the presence of cloud in the IR window imagery and to compute an absolute humidity from the satellite-derived upper tropospheric humidity (UTH), a measurement of the temperature profile above the ground is required. Upper-air meteorological data used for this purpose in this study consists of mean monthly rawinsonde data from Antofagasta (23.4°S, 70.4°W) for 00UT and 12UT. These mean profiles are based on a 10-year (1977-1986) average. The data are for pressure levels from the surface to 200mb at 50mb increments. Means and standard deviations of geopotential height, temperature, mixing ratio and component winds are provided for each level.

4.3 Climatology of the study period

The satellite analysis presented in this study is based on data collected in the period July 1993 to September 1999. Since telescopes remain in use for much longer periods, it is important to assess the study period in terms of long-term trends and inter-annual climate variability. For this purpose the National Center for Environmental Prediction (NCEP) and National Center for Atmospheric Research (NCAR) reanalysis data set was used (Kistler *et al*, 2001). This data set is a retroactive reconstruction of atmospheric parameter fields extending back 40 years or longer. Historical data from all possible sources were collected and added to existing databases. Data then underwent an extensive quality control. An assimilation scheme, kept constant over the reanalysis period, was then used to interpolate the observations to a global grid. A CD-ROM containing 41 (1958-1998) years of selected monthly fields has been produced from the full resolution data set.

Included on the CD-ROM are parameters that are directly or indirectly related to cloud cover and water vapor. Out-going Long-wave Radiation (OLR) at the top of the atmosphere, 500 mb and 300mb specific humidity (q) are three such parameters that were used in the climate analysis discussed below. OLR (Wm^{-2}) is inversely related to cloud cover. Increased cloud cover will reduce OLR reaching the top of the atmosphere from the earth's surface and *vice versa*. The specific humidity, the mass of water vapor (g) in a kilogram of air, differs from the water vapor mixing ratio (see section 2.3.3) by only a few percent. It may therefore be used to compute the PWV (equation 8). Using the 500mb and 300mb specific humidity the slope of the specific humidity versus pressure (height) curve is determined. The slope is maintained for pressures below 300mb to the level where the specific humidity reaches zero (typically around the 200mb pressure level). Integrating vertically, the PWV for the atmosphere above the 500mb pressure level (~5500m) is computed. In this section, when referring to PWV, this layer is implied.

In the analysis that follows, mean monthly values of OLR and PWV over the 41-year period from 1958 to 1998 were used. The mean monthly OLR and PWV were processed in two ways. Firstly the 12-month running mean was computed to remove the seasonal cycle and these data were used to determine the 41-year trend. Secondly, the monthly anomalies were determined by subtracting the long-term mean for a given month from the individual monthly values. The root mean square (RMS) difference between the individual monthly means and the long-term mean is used as an indicator of the inter-annual variability.

Four grid points were selected within the study area: 22.5°S, 67.5°W (North), 25.0°S, 67.5°W (Middle), 27.5°S, 67.5°W (South), and 27.5°S, 70.0°W (South-West). The data for all four points were analyzed, however, since differences across the region

were found to be small, only the results from the North and South points are presented graphically below. The key statistics are shown in Table 6 and 7 for all locations. The trend and anomaly plots for OLR are shown in Figures 11 and 12 and for PWV in Figures 13 and 14.

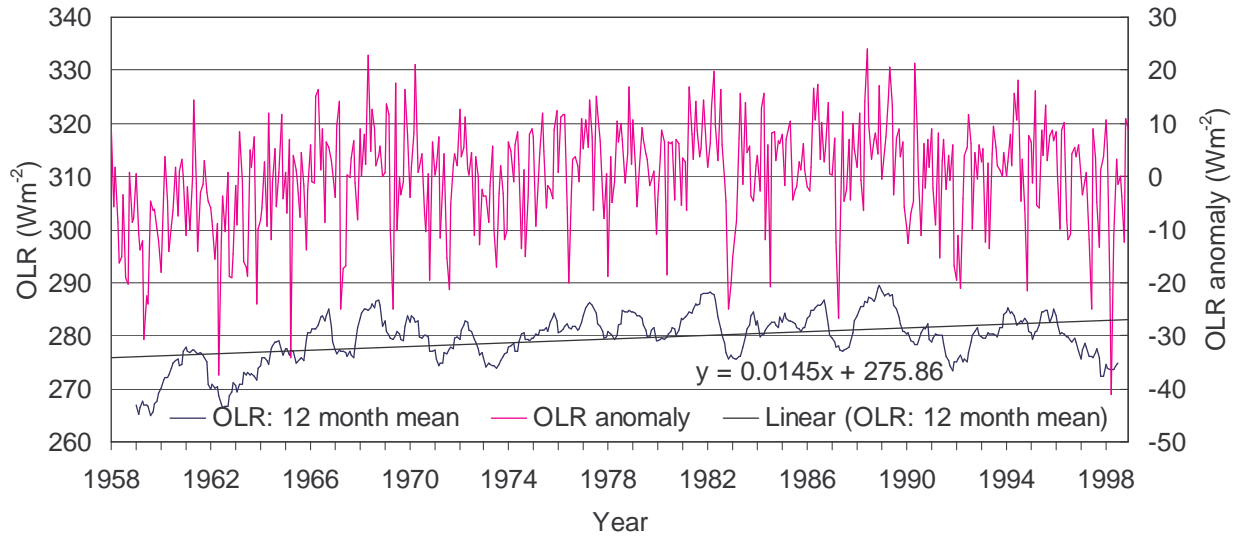


Figure 11. Out-going long-wave radiation (OLR): 12-month mean, 41-year trend and anomaly at 22.5°S, 67.5°W (North)

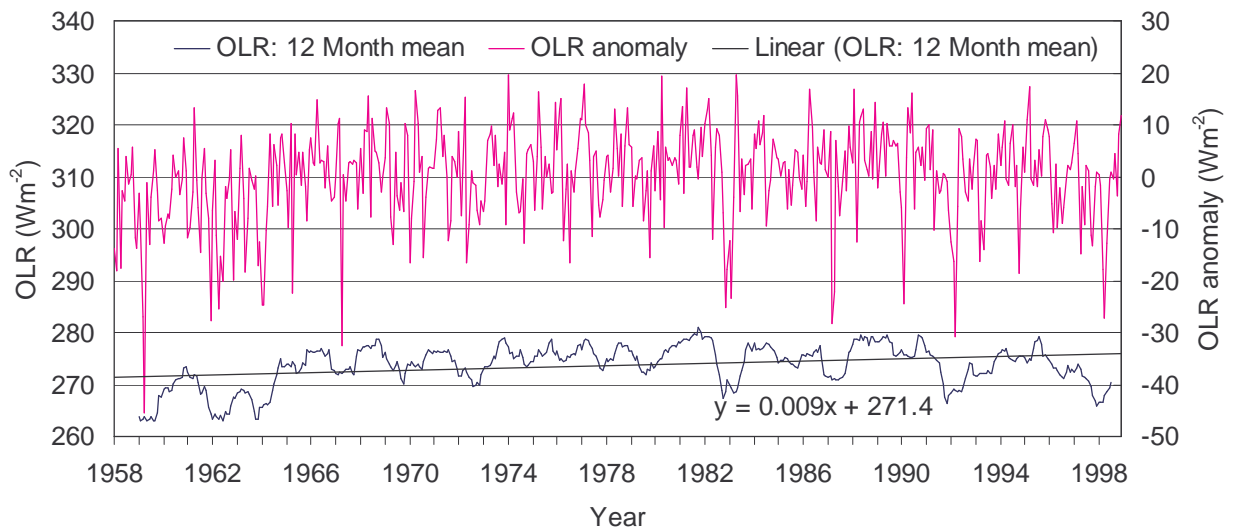


Figure 12. Out-going long-wave radiation (OLR): 12-month mean, 41-year trend and anomaly at 27.5°S, 67.5°W (South)

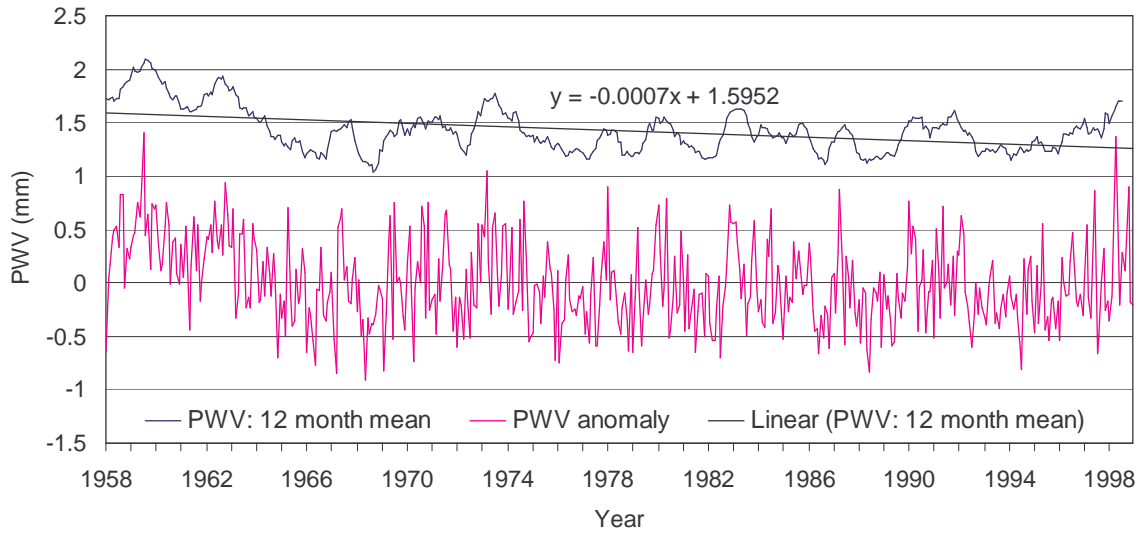


Figure 13. PWV: 12-month mean, 41-year trend and anomaly at 22.5°S, 67.5°W (North)

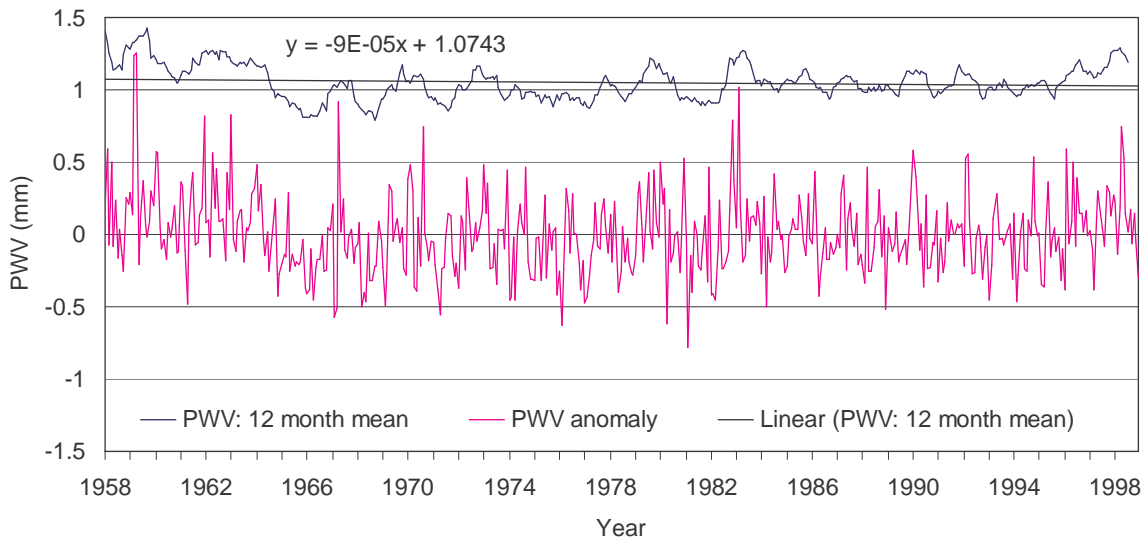


Figure 14. PWV: 12-month mean, 41-year trend and anomaly at 27.5°S, 67.5°W (South)

The long-term (41-year) trend in OLR is upwards at both locations but this trend should be interpreted with caution. Accurate determination of the OLR is greatly enhanced if satellite observations are used. If the trend-line is based on data collected after the advent of satellite observations (1978-1998), the trend is reversed at both locations (Figures 15 and 16).

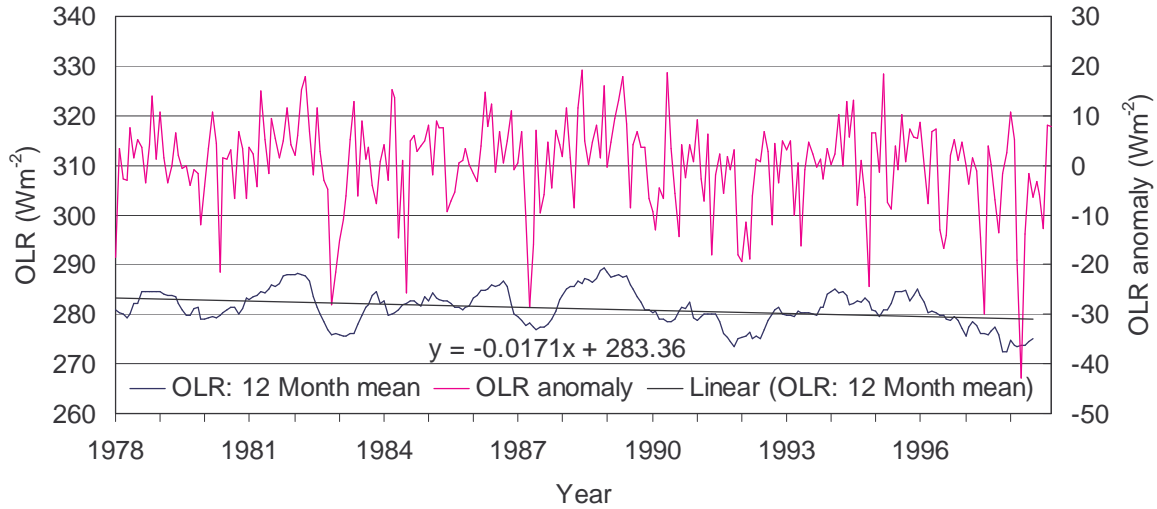


Figure 15. Out-going long-wave radiation (OLR): 12-month mean, 21-year trend and anomaly at 22.5° S, 67.5° W (North)

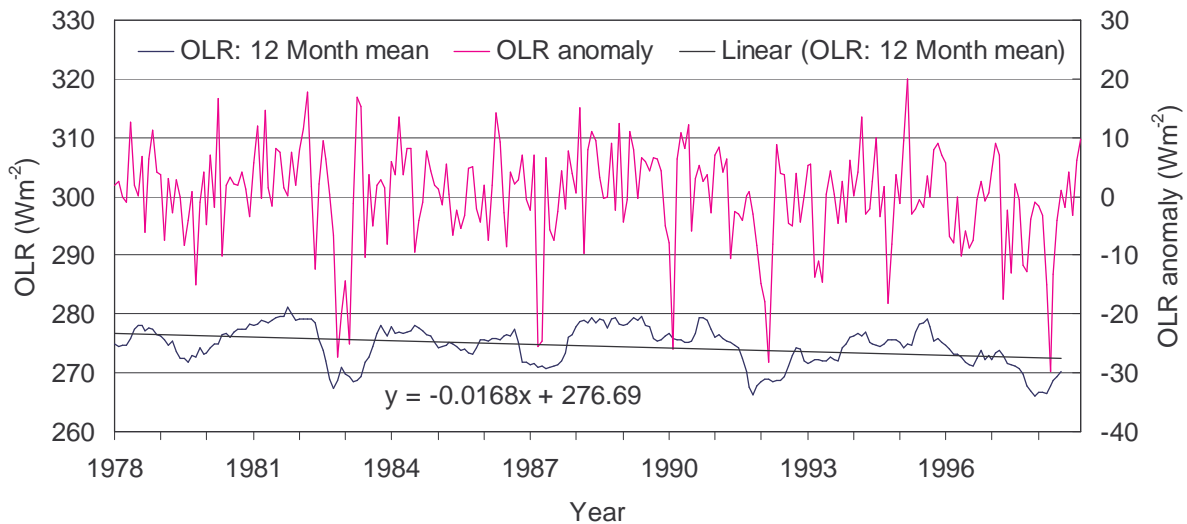


Figure 16. Out-going long-wave radiation (OLR): 12-month mean, 21-year trend and anomaly at 27.5° S, 67.5° W (South)

For PWV the NCEP reanalysis is expected to be more reliable further back in time than for OLR since satellite observations would be less critical for accurate moisture measurement in these data. Both the 41-year and 21-year trends are basically flat for PWV at both locations. The 21-year trend in OLR (downward) is consistent with the slight upward trend in PWV over the same period (Figures 17 and 18).

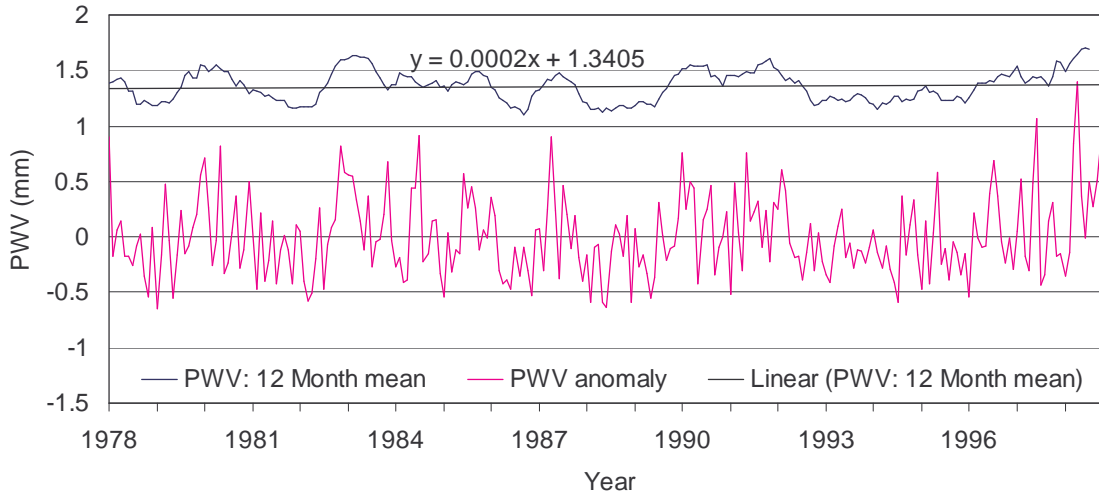


Figure 17 PWV: 12-month mean, 21-year trend and anomaly at 22.5°S, 67.5°W (North)

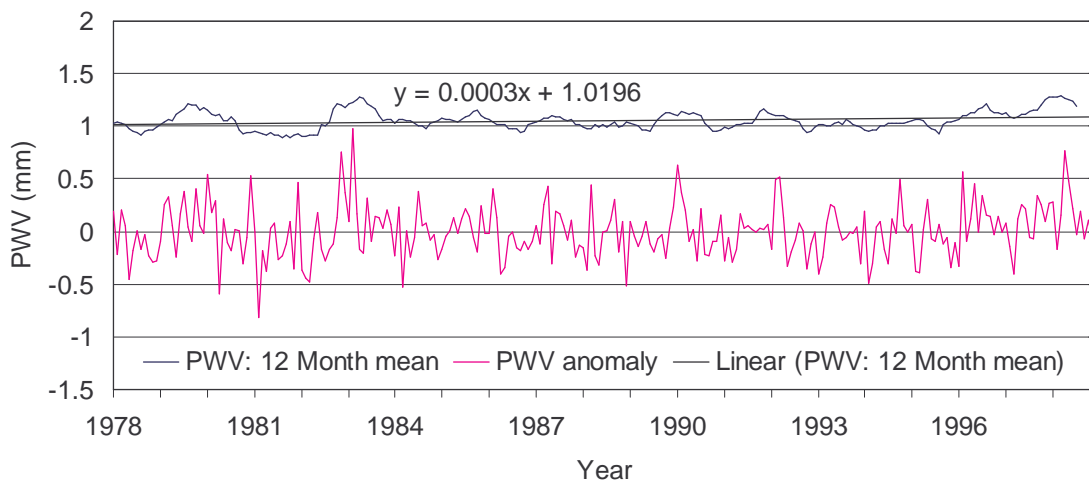


Figure 18. PWV: 12-month mean, 21-year trend and anomaly at 27.5°S, 67.5°W (South)

It is evident in both the OLR and PWV plots that inter-annual variability is large compared to the long-term trends. An interesting feature detected in the OLR anomaly plots is the periodic occurrence of large negative anomalies. Similarly large positive anomalies are not observed. These appear to coincide with El Niño events. Considering the monthly anomaly plots this relationship is not clear since positive OLR anomalies also occur during an El Niño. However, when the 12-month running mean of the OLR is plotted against the 12-month running mean of the Southern Oscillation Index (SOI) the relationship is apparent (Figure 19). The need to use the 12-month running mean makes sense when one considers that ENSO is a climate phenomenon and should therefore be expected to impact cloudiness at climate time-scales. This is an interesting discovery worthy of further study since the relationship implies that ENSO forecasts may be used to provide long-range climate forecasts of cloudiness and PWV at sites such as Chajnantor.

A significant feature in the PWV anomaly plots is the larger PWV variability (note excursions above 0.5 mm) at the North location compared to the South location. These tend to occur during El Niño events (Figure 20).

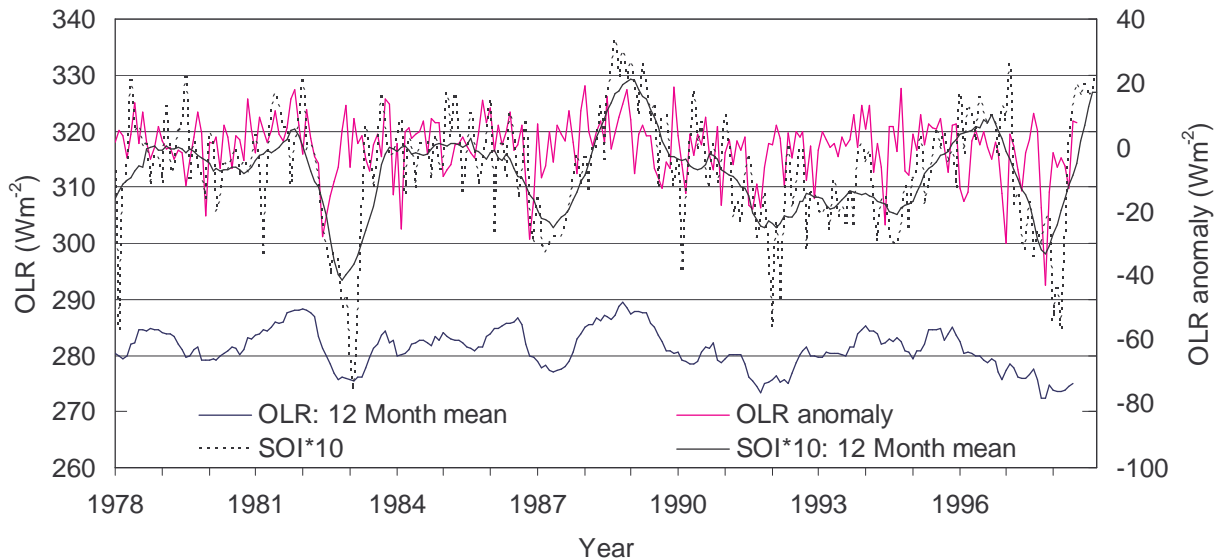


Figure 19. Out-going long-wave radiation (OLR) at 22.5°S, 67.5°W (North) and Southern Oscillation Index (12-month means and monthly anomalies).

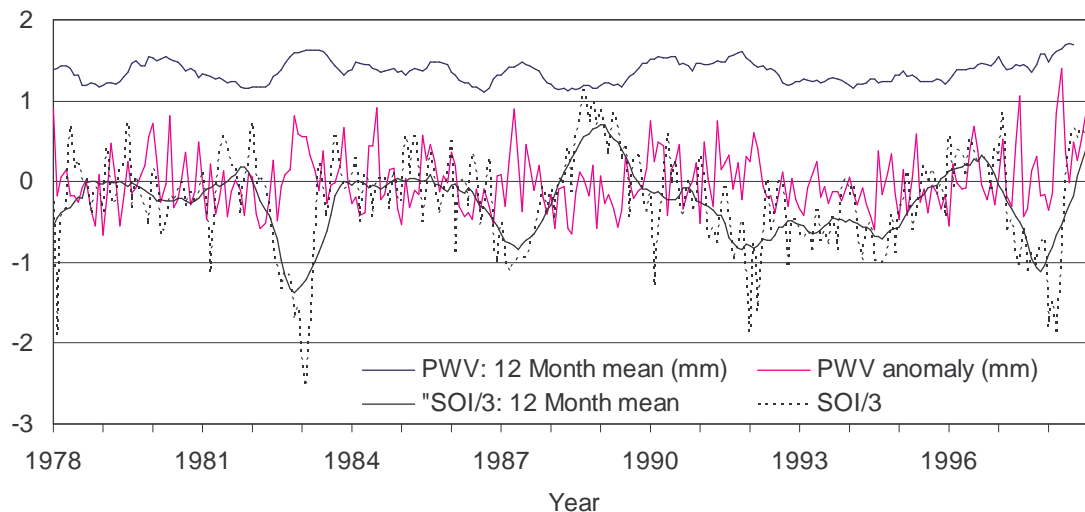


Figure 20. PWV at 22.5°S, 67.5°W (North) and Southern Oscillation Index (12-month means and monthly anomalies).

Key OLR and PWV statistics are shown in Tables 6 and 7 respectively for the 41-year period (1958-1998), 21-year period (1978-1998) and the study period (July 1993 – September 1999). RMS values were determined using the 41-year mean.

Table 6. OLR (Wm^{-2}) means and variability at four locations in the study area

Location	58-98 Mean	78-98 Mean	93-99 Mean	58-98 RMS	78-98 RMS	93-99 RMS
N (22.5°S,67.5°W)	279.3	281.1	280.2	10.0	9.7	10.3
M (25.0°S,67.5°W)	277.0	278.6	277.7	9.7	9.3	9.3
S (27.5°S,67.5°W)	273.5	274.6	273.7	9.1	8.6	8.0
SW (27.5°S,70.0°W)	271.5	272.4	271.2	8.8	8.2	7.6

Table 7. PWV (mm) means and variability at four locations in the study area

Location	58-98 Mean	78-98 Mean	93-99 Mean	58-98 RMS	78-98 RMS	93-99 RMS
N (22.5°S,67.5°W)	1.43	1.37	1.36	0.40	0.37	0.40
M (25.0°S,67.5°W)	1.23	1.20	1.20	0.33	0.30	0.29
S (27.5°S,67.5°W)	1.05	1.06	1.06	0.27	0.25	0.25
SW (27.5°S,70.0°W)	1.04	1.05	1.06	0.27	0.24	0.25

Given the questionable reliability of pre-1978 OLR values, it is prudent to base an assessment of the study period on a comparison with the period 1978-1998. In terms of variability within the study period, for both OLR and PWV, the RMS values for the study period are similar to long-term values. Variability decreases from north to south over the study area. This is the case for OLR and PWV. Mean OLR during the study period was lower than the long-term (1978-1998) mean at all the locations by about the same amount ($\sim 1 \text{ Wm}^{-2}$).

To obtain a first order assessment of the relationship between OLR values and cloud cover, monthly OLR and clear fraction data were analyzed for the study period. The monthly clear fraction anomalies for Chajnantor and Chalviri were compared to the monthly OLR anomalies for the closest grid point in the NCEP data domain (22.5°S, 67.5°W). It is clear from Figure 21 that, on a month-to-month basis, there is not exact correspondence between the clear fraction anomaly and OLR anomaly. This is not unexpected since the satellite measurement is based on cloud cover above the observatory at 10km resolution while the OLR is for the grid point location in the NCEP data domain at 2.5° resolution. Additionally, surface altitude is different and the locations are separated by a distance of about 60km. The usefulness of the comparison lies in assessing average (climatological) conditions over the entire study period. For this reason the RMS difference between the individual monthly means and the *monthly means for the study period* were computed. Table 8 shows the RMS values. Typically, an OLR anomaly of 1 Wm^{-2} corresponds to a cloud cover anomaly of about 1%. Therefore, according to the data in Table 6, it is suggested that the clear fraction is being underestimated at *all* the sites by about 1% during the study period.

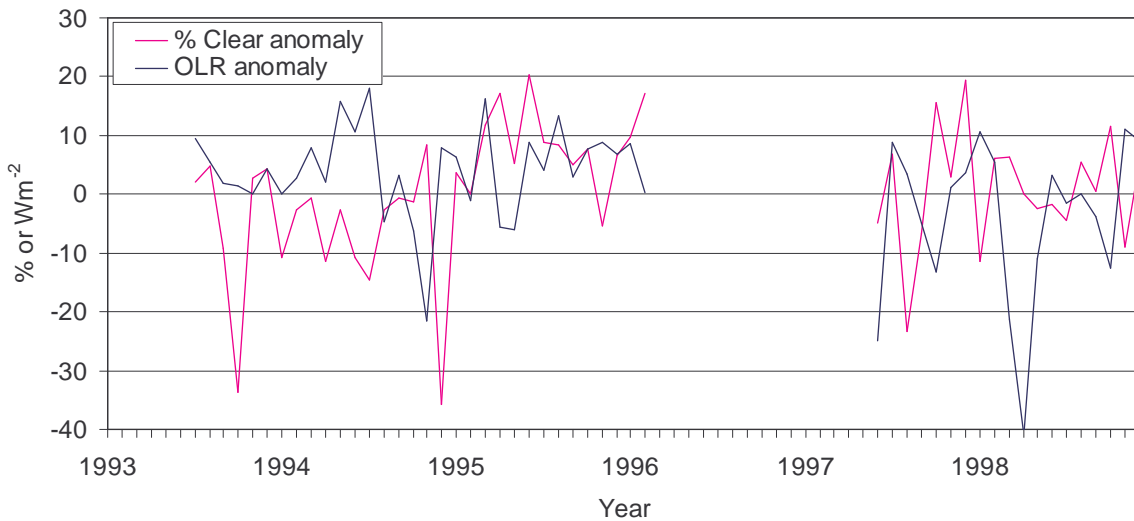


Figure 21. Monthly clear fraction and OLR anomalies at Chajnantor during the study period.

Table 8. RMS OLR and clear fraction anomalies for the study period

Parameter	RMS
NCEP (22.5°S, 67.5°W) OLR RMS anomaly (Wm^{-2})	9.7
Chajnantor RMS Clear fraction anomaly (%)	9.7
Chalviri RMS Clear fraction anomaly (%)	9.2

The RMS of the clear fraction anomalies for the study period allows for an additional assessment of cloud cover variability at each of the sites being compared. Table 9 shows these values. Differences are small but an interesting observation is that variability increases to the south and west. This is opposite to what was detected using the OLR anomalies. The clear fraction anomalies based on the satellite data are probably unrepresentative. Since the satellite cloud data covers only five years, computation of the monthly means and anomalies is based on between four and six values.

Table 9. RMS clear fraction anomalies at each site for the study period

Site	RMS Clear fraction anomaly (%)
Chajnantor	9.7
Chalviri	9.2
Arg High	10.8
Arg Mid	10.4
Arg South	10.5
Arg Low	10.4
Arg West	12.8

For PWV derived from the NCEP reanalysis data (Table 7) the mean and RMS variability for the study period is almost identical to the long-term mean and variability. Based on this fact, it is concluded that PWV, as measured during the study period, is representative of long-term moisture conditions.

Table 10 shows the RMS variability for PWV at each site using satellite measurements for the study period. The NCEP PWV (above 500 mb) variability for the closest grid point over the same period is shown in parentheses in the table. Differences are generally small but the site that is significantly lower (Arg Low) than the others has a noticeably larger variability. There is some indication that variability increases from north to south which is the same trend observed in the satellite cloud cover data. Chajnantor is an exception to this trend. This may be due to local effects produced by the Salar de Atacama (Erasmus and van Staden, 2001).

Table 10. Satellite PWV RMS anomalies at each site for the study period (figures in parentheses are for the nearest NCEP grid point)

Site	RMS PWV anomaly (mm)
Chajnantor	0.31 (0.37)
Chalviri	0.28 (0.37)
Arg High	0.28 (0.26)
Arg Mid	0.32 (0.26)
Arg South	0.33 (0.21)
Arg Low	0.43 (0.26)
Arg West	0.30 (0.26)

4.4. Site comparison: Cloud cover

The methodology used to determine sky cover conditions is described in section 2.3. In the analysis that follows, “clear” conditions are those when the 9-pixel area (section 2.4) used to determine sky cover above the site is completely free of all cloud, including transparent cirrus (ice) cloud. “Useable” conditions are those when the 9-pixel area is either free of cloud or has some fraction of transparent cirrus (categories I1, I2 & I3) but is free of all clouds containing liquid water. The sites selected for comparison were analyzed in terms of overall conditions, seasonal variability and diurnal variability. Overall conditions and seasonal variability are based on observations over a full 24-hour day. For diurnal variability, four day-night periods were used as defined in section 2.3.

4.4.1 Overall conditions

The fraction of the time that conditions are clear and useable is shown in Figure 22. As may be expected, since the sites are in relatively close proximity to one another, sky cover differences are subtle. It is readily apparent that the sites located further south (Arg Mid and Arg South) are more cloudy. Arg West is the clearest site.

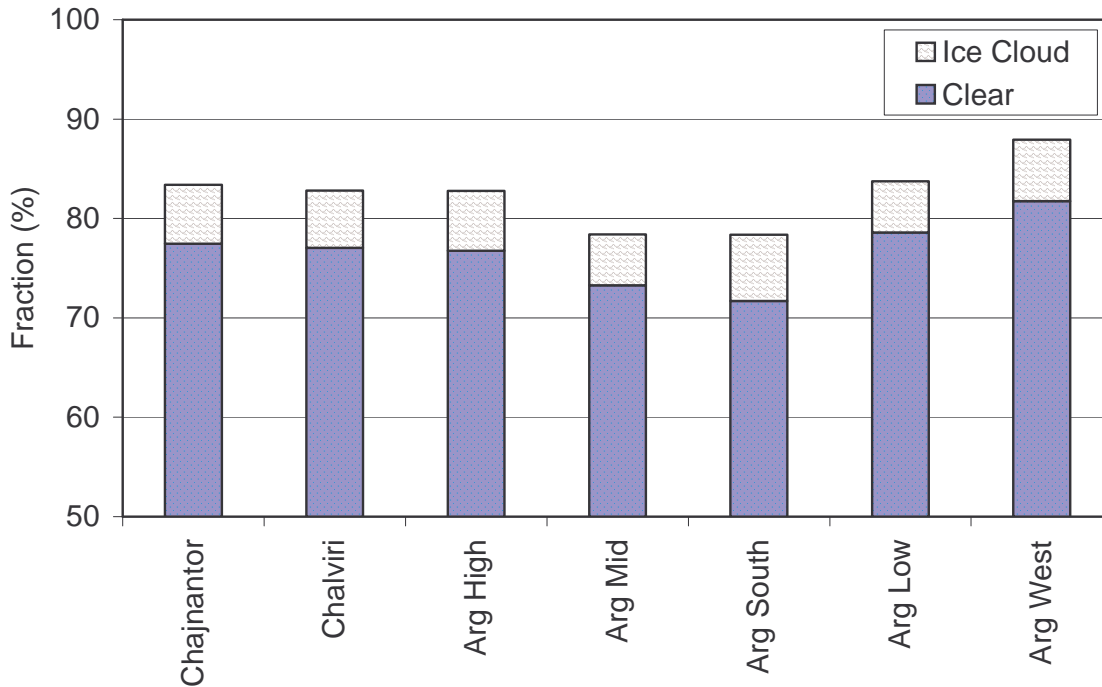


Figure 22. Fraction of time that sky cover conditions are clear and useable (includes transparent ice cloud) for a 24-hour observing day.

4.4.2 Seasonal variations

The seasonal distribution of the fraction of useable conditions for a 24-hour observing day at each site is presented in Figure 23. The northern sites are clearest in Winter and Spring with a noticeable increase in cloudiness in the Summer. In the south, Winter is most cloudy and the summer is relatively clear.

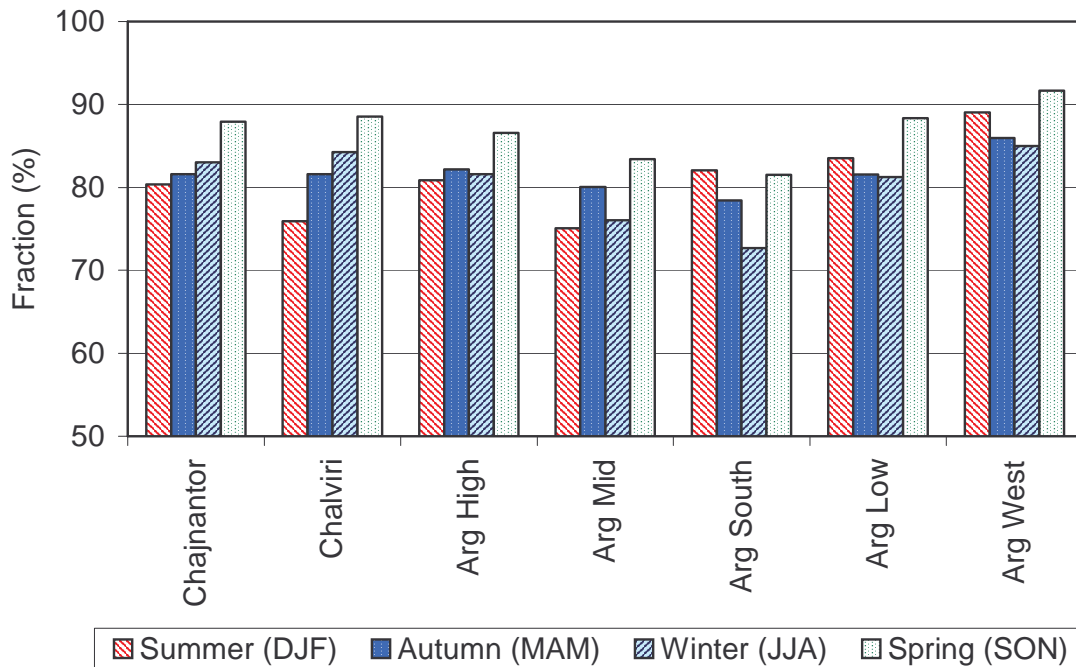


Figure 23. Fraction of time that sky cover conditions are useable (clear plus transparent ice cloud) for a 24-hour observing day by season.

4.4.3 Diurnal variations

Daily variations in cloud cover are shown for each site by season in Figure 24. The largest variations during the day are observed in Summer in association with the convective cycle. Strong surface heating at this time of the year results in the formation of clouds in the afternoon which may develop further into thunderstorms. This generally occurs east of the Andes where the atmosphere is unstable and abundant moisture is present at low levels. When thunderstorms occur, widespread cloud cover occurs in the outflow region of these storms in the upper troposphere. The upper level circulation accompanying these storms results in the movement of clouds from the east towards and sometimes across the Andes. Local convection can also produce afternoon cloud at the sites but these dissipate soon after sunset. Therefore, clearing is observed in the first half of the night. Where movement of cloud from the east is likely, clearing is halted or reversed. This is the case at the more northern sites (Chajnantor and Chalviri). In the south, clearing continues through the night since the upper level flow is more consistently from the west.

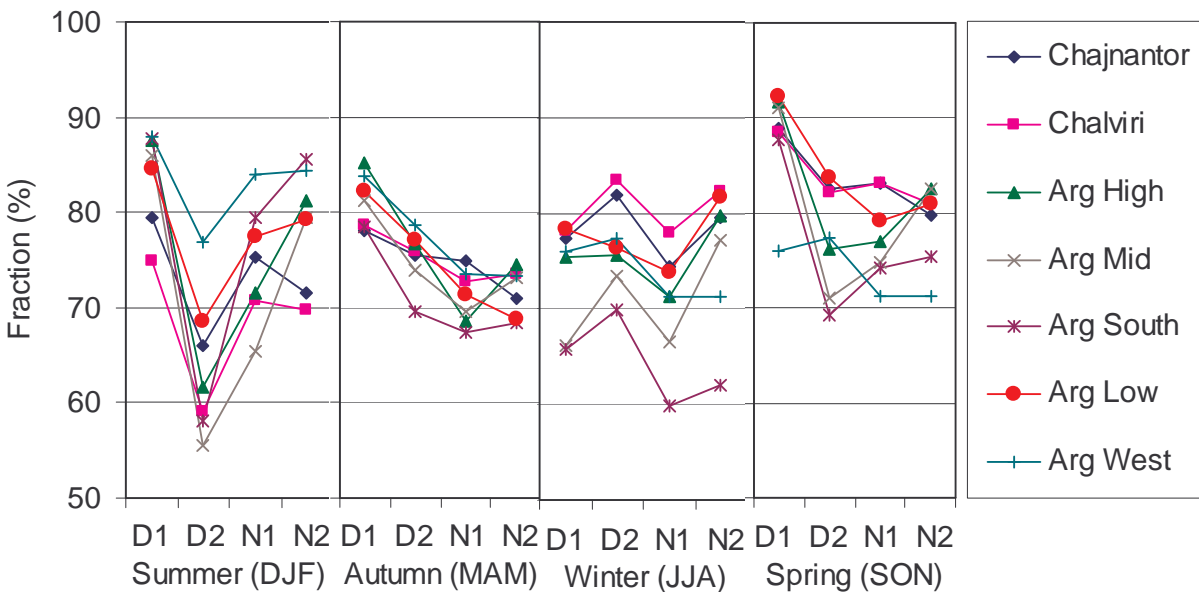


Figure 24. Fraction of time that sky cover conditions are clear for different periods of the day by season.

In the Autumn months convection, particularly local convection, is suppressed. However, some convective activity persists into the early Autumn east of the Andes and cloud may move over the sites in the afternoon and at night from this source. Thus afternoon and night-time cloudiness would be enhanced. In Winter, cloud producing mechanisms are associated with mid-latitude frontal cyclones. Sites located further south are influenced more by these storms. At almost all the sites a maximum in the clear fraction is observed in the Day 2 and Night 2 periods and a minimum in the Day 1 and Night 1 periods. The reason for this observation is not readily apparent. A possible explanation relates to the fact that, even in Winter, during the day, the ground surface in the Andes is warmer than the air. The cloud produced by frontal storms at and above the altitude of the sites is typically stratiform in nature. If a stratiform a cloud layer were to move over such a heated surface,

convective cloud elements would form in the layer, enhancing cloudiness. It is reasonable that such enhanced cloudiness would peak after sunset since the sites are located east of where this enhancement occurs. Such an event which occurred on 10 August 1998 was documented in Erasmus and van Staden (2001).

4.4.4 Ranking of sites: cloud

For a 24-hour observing day, a ranking of the 6 sites was carried out based, respectively, on:

- (i) the clear fraction and
- (ii) the useable (clear plus transparent ice cloud) fraction.

The ranking is done by dividing the range of values (clear fraction or useable fraction) into 6 equal intervals. 7 bins were defined with the fraction of the clearest site at the center-point of bin 1 and the fraction of the cloudiest site at the center-point of bin 7. Sites are then ranked from 1 (clearest) to 7 (most cloudy) depending on the bin in which the clear or useable fractions falls. The ranking is shown in Table 11.

Table 11. Clear and useable (clear plus transparent ice cloud) fractions for a 24-hour observing day and site quality ranking based on cloud cover conditions.

No	Site	Clear Fraction	Rank	Useable Fraction	Rank
1	Chajnantor	0.775	4	0.834	4
2	Chalviri	0.770	4	0.828	4
3	Arg High	0.768	4	0.828	4
4	Arg Mid	0.733	6	0.784	7
5	Arg South	0.717	7	0.784	7
6	Arg Low	0.786	3	0.837	4
7	Arg West	0.818	1	0.879	1

4.5 Site comparison: PWV

The methodology used to compute the precipitable water vapor (PWV) from satellite observations at $6.7\mu\text{m}$ is described in section 2.3.5. A requirement for the measurement of PWV is that no clouds are present in the 9-pixel site area. As explained in section 2.3.3, in order to avoid problems caused by cold elevated land surfaces, the PWV analysis and comparison is based on day-time PWV values.

4.5.1 Overall conditions

PWV percentile values for the sites are shown in Figure 25 and the PWV frequency distributions in Figure 26. The dominant control for PWV is clearly altitude. This is the case since the scale height of water vapor in the atmosphere is small and because temperature, which determines the equilibrium vapor pressure, drops

sharply with altitude ($\sim 7^{\circ}\text{C}/\text{km}$). For sites at a similar altitude, differences in PWV are controlled by temperature as determined by site latitude.

Chalviri and Arg West are the driest sites being marginally better than Chajnantor due to their 200m higher altitude. These three sites are clearly superior to the other four sites. Figure 26 shows that at Chalviri, Arg West and Chajnantor, PWV is below 1 mm 50.3%, 45.9% and 42.3% of the time, respectively. Chajnantor and Arg High are similar but Chajnantor has lower 10th percentile and 1st quartile values. Arg Mid and Arg South are comparable but significantly poorer than the best 3 sites. Arg Low, although it has a fairly high clear fraction, performs worst in terms of PWV because of its low altitude (4400 m).

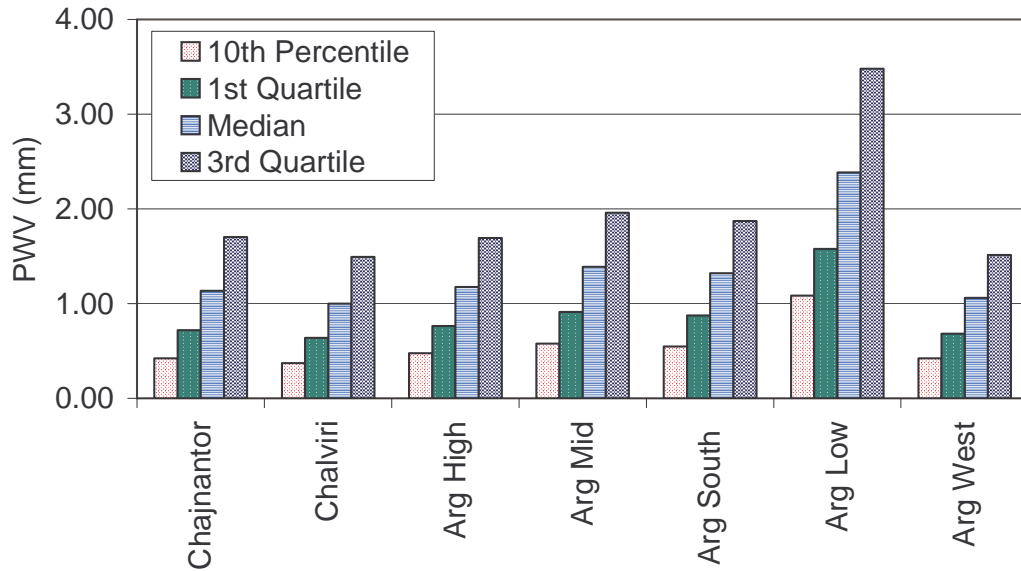


Figure 25. PWV percentile values at each site under clear conditions.

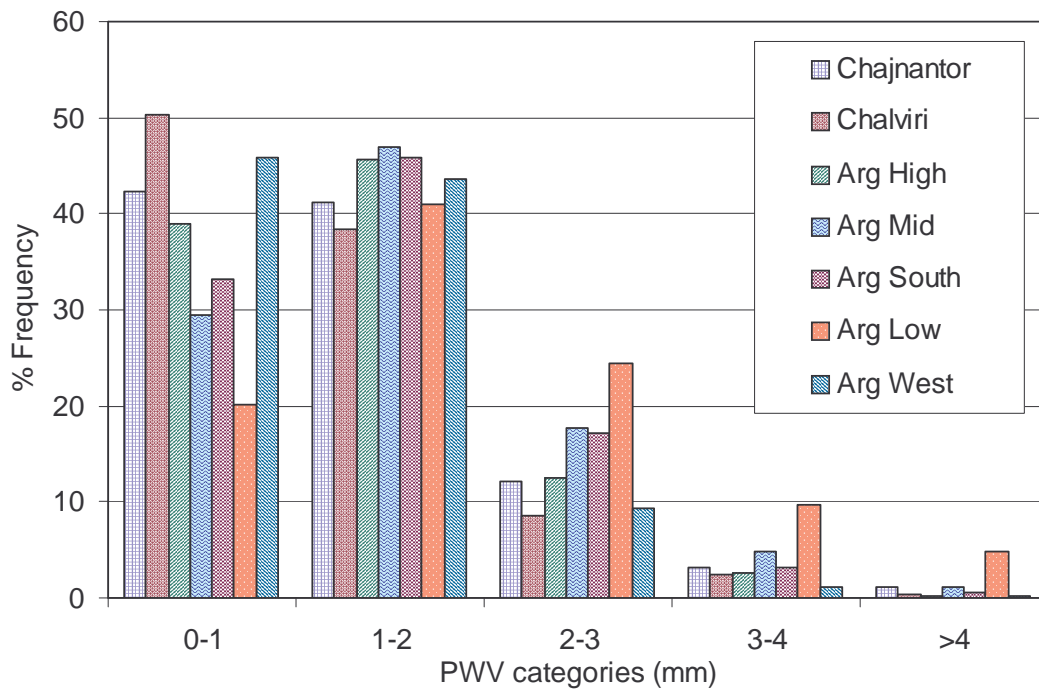


Figure 26. Frequency distribution of PWV values at each site under clear conditions.

4.5.2 Seasonal variations

Seasonal variation of water vapor, as indicated by the median PWV, is shown in Figure 27. Seasonal variations are generally small. The seasonal temperature cycle is the main control, with the result that Winter and Spring are the driest seasons with Summer and Autumn the most humid.

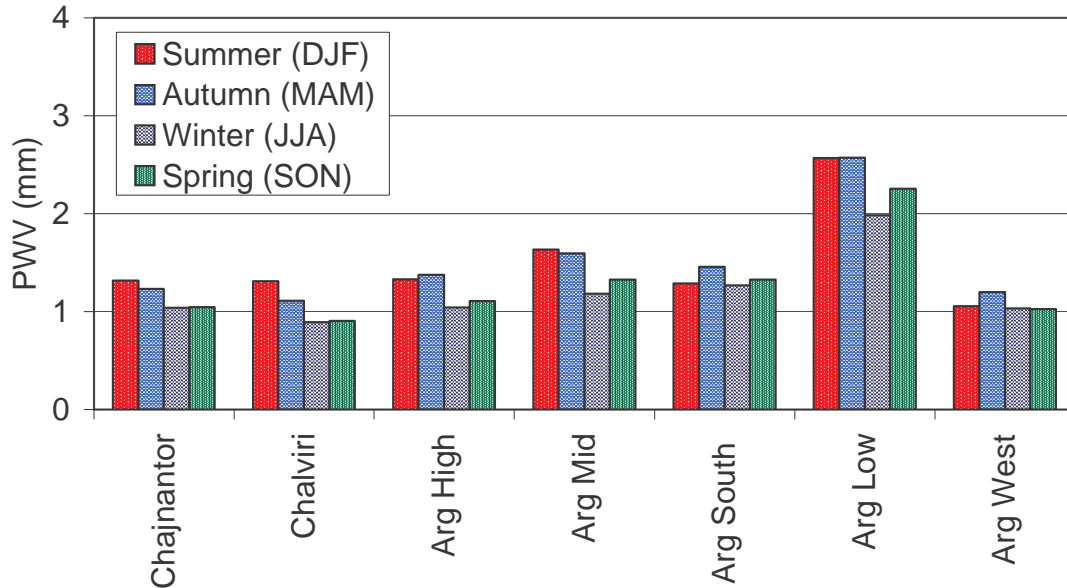


Figure 27. Seasonal distribution of median PWV values at each site under clear conditions.

4.5.3 Ranking of sites: water vapor and cloud cover

As noted above, water vapor conditions must be considered in the context of the cloud cover analysis since the PWV measurements are only made when it is clear. Therefore, if two sites have similar PWV distributions, the site with the larger clear or usable (clear plus transparent ice cloud) fraction is superior. In devising figures of merit for the sites in terms of water vapor conditions, these figures weight the PWV values using the usable fraction at each site. The PWV values and corresponding usable fractions were divided by season of the year in the computations. Two figures of merit based on the median and 10th percentile values of PWV were derived for each site as follows:

$$Q1 = (1/PWV_{\text{median}})(\text{Useable fraction})(100)$$

$$Q2 = (1/PWV_{10\text{th Percentile}})(\text{Useable fraction})(Q1_{\text{mean}}/Q2_{\text{mean}})(100)$$

Q2 is normalized using the means for Q1 and Q2 at all the sites. Thus Q1 and Q2 are considered to have equal weight. The ranking is determined by dividing the range of values into 6 equal intervals. 7 bins were defined with the largest Q-value at the center-point of bin 1 and the lowest Q-value at the center-point of bin 7. Sites are then ranked from 1 to 7 depending on the bin in which the Q-value for the site falls. Q-values were computed for a full 24-hour observing day, for daytime only and nighttime only. To better facilitate comparison of the sites, all the Q-values were divided by the Q-value for Chajnantor. The 10th percentile and median PWV values,

Q-values and site ranking are shown in Table 12 for a 24-hour observing day. Table 13 shows the Q-values and ranking separately for day and night.

Table 12. PWV percentile values (mm), figures of merit for site quality and site ranking based on PWV weighted by the useable (clear plus transparent ice cloud) fraction.

No	Site	Median	Q1	10%ile	Q2	QS	Rank
1	Chajnantor	1.13	1.00	0.42	1.00	1.00	2
2	Chalviri	1.00	1.11	0.37	1.15	1.13	1
3	Arg High	1.18	0.95	0.48	0.88	0.92	3
4	Arg Mid	1.39	0.77	0.58	0.70	0.73	5
5	Arg South	1.32	0.81	0.55	0.75	0.78	4
6	Arg Low	2.38	0.50	1.08	0.41	0.45	7
7	Arg West	1.06	1.13	0.42	1.06	1.09	1

Table 13. Figures of merit for site quality and site ranking based on PWV weighted by the daytime and nighttime useable (clear plus transparent ice cloud) fraction.

No	Site	Daytime				Nighttime			
		Q1	Q2	QS	Rank	Q1	Q2	QS	Rank
1	Chajnantor	1.00	1.00	1.00	2	1.00	1.00	1.00	2
2	Chalviri	1.10	1.14	1.12	1	1.12	1.16	1.14	1
3	Arg High	0.96	0.89	0.92	3	0.94	0.87	0.91	3
4	Arg Mid	0.77	0.70	0.74	4	0.76	0.69	0.72	5
5	Arg South	0.81	0.74	0.77	4	0.81	0.75	0.78	4
6	Arg Low	0.50	0.42	0.46	7	0.49	0.40	0.44	7
7	Arg West	1.12	1.06	1.09	1	1.13	1.06	1.09	1

5. Summary and conclusion

Cloud cover and water vapor conditions at Chajnantor (Chile), Chalviri (Bolivia) and five sites in Argentina have been analyzed using satellite observations totaling approximately five years of data between July 1993 and September 1999. The sites are located on the Andean Altiplano in the area of Northern Chile, Bolivia and Argentina within 20.5°S to 30.5°S and 66.0°W to 72.0°W.

The sites were analyzed, compared and ranked in terms of observing quality. Since the sites were evaluated for the ALMA project cloud cover was divided into transparent cirrus (ice) cloud and opaque cloud. Usable conditions were defined as those when it is clear or when some fraction of transparent cirrus (ice) cloud is present. All opaque cloud conditions were considered unuseable since liquid water cloud droplets are either positively or probably present under these conditions. The

other critical parameter for ALMA operations is PWV above the sites. Key PWV statistics were determined from the satellite measurements of PWV for each site. The 10th percentile and median PWV values were used in combination with the cloud cover information to compute a figure of merit for each site and then to rank the sites.

The main factors determining site quality are the altitude of the site and position in relation to the climatological distribution of cloud cover. Accordingly, the sites with the optimal combination of dry and clear conditions are the sites with the highest elevation and furthest west location. A clear division in quality was found between the four best sites (Chalviri, Chajnantor, Arg High and Arg West) and the other three sites (Arg Mid, Arg South and Arg Low). Considering the four best sites, when compared to Chajnantor, Chalviri and Arg West are about 10% better and Arg High about 10% worse. Chalviri and Chajnantor have almost identical cloud cover but the former is drier. Chajnantor and Arg West have nearly the same PWV but the latter is clearer.

9. References

Delgado, G., A. Otarola, V. Belitsky, D. Urbain, R. Hills and P. Martin-Cocher, 1999: The Determination of Precipitable Water Vapour at Llano de Chajnantor from Observations of the 183 GHz Water Line. ALMA Memo 271.1

Erasmus, D.A. and D.S. Maartens, 1999: Operational Forecasts Of Cirrus Cloud Cover And Water Vapor Above Paranal And La Silla Observatories. European Southern Observatories Report under contract number 52538/VPS/97/9480/HWE.

Erasmus, D.A. and D.S. Maartens, 2001: Maintenance, Upgrade and Verification of Operational Forecasts of Cloud Cover and Water Vapor above Paranal and La Silla Observatories. European Southern Observatories Report under contract number 58311/ODG/99/8362/GWI/LET.

Erasmus, D.A. and M. Sarazin, 2000a: Forecasting Precipitable Water Vapor and Cirrus Cloud Cover For Astronomical Observatories: Satellite image processing guided by synoptic model dissemination data. SPIE Conference on Image and Signal Processing for Remote Sensing IV. Paper SPIE-4168, Barcelona. 25-29 September, 2000.

Erasmus, D.A. and M. Sarazin, 2002: Utilizing Satellite Data For Evaluation and Forecasting Applications At Astronomical Sites. IAU Technical Workshop: Astronomical Site Evaluation in the Visible and Radio Range. Marrakesh, Morocco, 13-17 November, 2000. Astronomical Society of the Pacific Conference Series. Vol. 266, 310-326.

Erasmus, D.A. and C.A. van Staden, 2001: A Satellite Survey of Water Vapor and Cloud Cover in Northern Chile. Final Report. Cerro-Tololo Inter-American Observatory.

Erasmus, D.A., and C.A. van Staden, 2002: A Satellite Survey of Water Vapor and Cloud Cover in the South-western U.S.A. and Northern Mexico. Final Report. The CELT Project and Aura Inc. 54pp.

Wallace, J.M. and P.V. Hobbs, 1977: *Atmospheric Science: An Introductory Survey*. Academic Press, New York, 467pp.

Appendix

Time series plots of PWV at Chajnantor over the period October 1998 – December 1999 as measured by the satellite (SatPix) and the ESO 183 GHz radiometer (ESO20). Only synchronous pairs of observations are shown for clear conditions. The radiometer measurement is a 20 minute average centered on the time the satellite is scanning Chajnantor. The satellite measurement is based on the 8 km x 8 km pixel closest to Chajnantor. For more details see section 3.2.

